Numerical Analysis of Micro Vortex Generators on Ramp Induced Shock/Boundary Layer Interaction

a project presented to
The Faculty of the Department of Aerospace Engineering
San José State University

in partial fulfillment of the requirements for the degree
Master of Science in Aerospace Engineering

by

Jeffrey Carruth

December 2018

approved by

Dr. Periklis Papadopoulos
Faculty Advisor

San José State
UNIVERSITY

ABSTRACT

Micro vortex generators (MVGs) are one of many tools that aerodynamicists have employed to improve aircraft performance and flow characteristics. They are tiny protrusions on a surface with a height roughly about the size of the expected boundary layer. These protrusions generate a vortex, sucking faster moving air into the boundary layer. When introduced in front of a shock wave, the shock wave weakens, making micro vortex generators a form of reducing wave drag.

Much research has been recently performed to investigate and optimize the effects that micro vortex generators have on shock waves. One of these investigations was performed in 2017 with the Mach number equal to 2.5 and the Reynold's number equal to 5760. Using this experiment as a benchmark, MVGs of varying heights were tested to further explore the resultant phenomenon and potentially determine an optimized height. The simulations were performed using ANSYS Fluent for both 2D and 3D cases. The 2D cases were simulated using a Reynolds-Averaged Navier-Stokes and Large Eddy Simulation solvers.

The 2D results demonstrated some interesting patterns with the LES simulations more accurately predicting flow conditions as have been observed in past experimental research. The 3D cases did not converge, most likely due to a low cell count. Further simulations and experiments are needed to accurately simulate the vortices and shocks generated. Repeat simulations for the 2D cases could also be performed or given more time to converge in order to further verify those results.

TABLE OF CONTENTS

LIST OF FIGURES

LIST OF TABLES

LIST OF SYMBOLS

Symbol	Definition	Units
a	Speed of Sound	m/s
e	Internal Energy	J
h	Height of MVG	m
k	Thermal Conductivity	W/(m*K)
M	Mach Number	-
P	Pressure	N/m^2
q	Heat Transfer Rate	W
R	Specific Gas Constant	J/(kg*k)
Re	Reynold's Number	-
U	Flow velocity	m/s
Abbreviations		
BL	Boundary Layer	-
CFD	Computational Fluid Dynamics	-
FEA	Finite Element Analysis	-
LES	Large Eddy Simulation	-
MVG	Micro Vortex Generator	-
RANS	Reynolds-Averaged Navier-Stokes	-
Greek Symbols		
γ	Ratio of Specific Heats	-
δ	Incompressible BL Nominal Thickness	m
$\delta*$	Incompressible BL Displacement Thickness	m
θ	Incompressible BL Momentum Thickness	m
μ	Dynamic Viscosity	kg/(m*s)
ρ	Density	kg/m^3
τ	Shear Stress	N/m^2
Subscript		
e	Edge of Boundary Layer	-
0	Stagnation Property	-

INTRODUCTION

1.1 MOTIVATION

Much research has recently been performed surrounding the use and effectiveness of micro vortex generators. While normal vortex generators are widely understood and used in subsonic flows, micro vortex generators in supersonic situations are still being investigated. This is due to the complex interaction of shock waves and boundary layers. Flow following a shock wave tends to separate rather quickly which disturbs the natural growth of the boundary layer and creates separation.

Shock waves are well known for generating wave drag and, as such, much investigation has gone into reducing this form of drag. Their interaction with the boundary layer, though, also adds to the overall drag of the object or aircraft. By placing a micro vortex generator in front of the shockwave, the boundary layer behind the wall is reinvigorated, and the pressure drag is reduced. This has been proven by numerous studies, including those performed by Pearcy (1961) who was one of the first to look into the issue. Pearcy (1961) studied the effect of control devices that would reduce flow separation after a shockwave on transonic airfoils with favorable results.

With the rise in technology, modern aerodynamicists such as Yan, Chen and Li (2017) have looked into the phenomenon with the ability of Computational Fluid Dynamics (CFD). Their recent experiments have used a simple inclined ramp to produce an oblique shock wave as opposed to a transonic airfoil. Building on past research, they tested a micro vortex generator at certain conditions to further examine and understand its effects on and after the shock wave. Their results agreed with those of past research.

While their experiment was well done, it assumed a certain height for the micro vortex generator based off research performed by Holden and Babinsky (2007). As this was an

assumption, the question of whether the height used was the optimal height for the experiment remains and has hence become the subject of investigation for this project. A review of micro vortex generators is provided to further expound on their nature as well as the research performed by Yan et al. (2017).

1.2 LITERATURE REVIEW

As the field of aerodynamics has progressed, new methods to improve and control flow characteristics have been discovered. One of these methods is the use of a vortex generator. Standard vortex generators are small protrusions or blades on the surface of a wing. In subsonic flow, these small protrusions generate a vortex which sucks in high energy air and mixes it with the more stagnant air of the boundary layer. This reduces the boundary layer and delays flow separation, effectively decreasing the pressure drag and allowing aircraft to fly at higher angles of attack before stalling. This effect can be seen in Figure 1 as the airfoil on the left, equipped with vortex generators, delays flow separation and greatly decreases the recirculation area.

Flap Equipped with SBVGs   Uncontrolled Flap
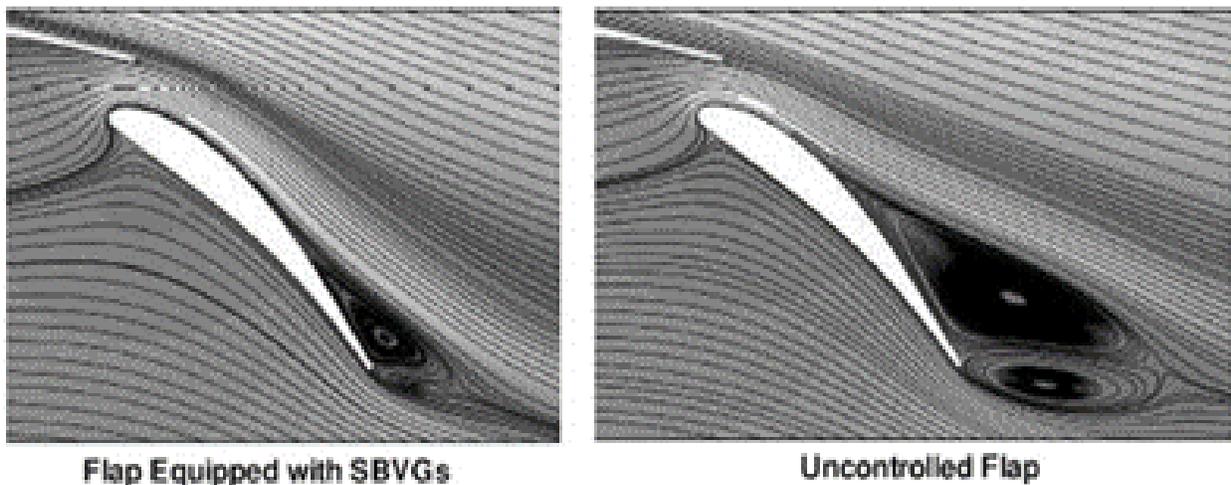
Figure 1 – Airfoil at high angle of attack. The airfoil at the left has MVGs while the one on the right does not (Meunier & Brunet, 2008).

Experimentation with vortex generators has concluded that, while effective at lower

speeds, they become much less efficient at higher velocities as the drag induced by the vortex

generators outweighs the benefit of separation delay (Titchener & Babinsky, 2015). Thus,

investigation into smaller vortex generators began. The result was what is known as micro vortex

generators (MVGs). These MVGs are the same as their larger counterpart but only protrude

slightly into the boundary layer, generally between 20-100% of the boundary layer height

(Titchener & Babinsky, 2015). This enables a vortex to generate within the boundary layer that

revitalizes the flow but does not have a large enough profile to induce an appreciable drag

penalty.

Many different geometries have been tested to try and find an optimal MVG design. As

there are many designs that have been tested they will not all be shown in this report. However, a

summary of the best performing designs is given, as presented by Titchener and Babinsky (2015)

in Figure 2.
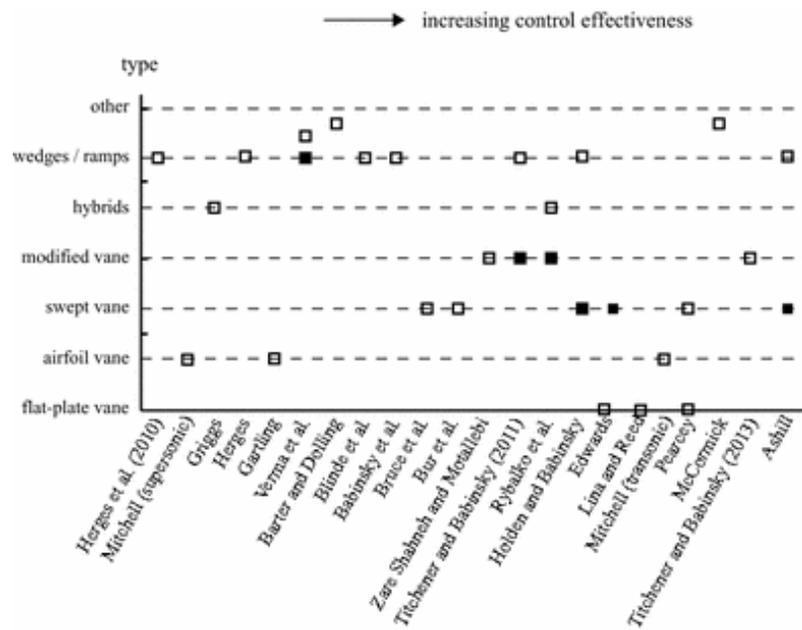
Figure 2 – Summary of performance for various geometries of MVGs (Titchener & Babinsky, 2015).

As shown in Figure 2, the three consistently best performing designs are the wedge/ramp, a swept vane and a modified vane. The first is a triangular ramp with the pointed end raised and pointed downstream. The second design option is two vanes situated similarly to the ramp where the vanes slant toward each other at the back end. A third option is a combination of the two which can be described as a ramp with a slat in the middle.

The performance of these geometries has yielded similar results with the vane type being marginally better than the other two (Titchener & Babinsky, 2015). However, due to the structural stability and feasibility of the ramp, this type has the greatest potential to be applied for real world situations (Panaras, & Lu, 2015).
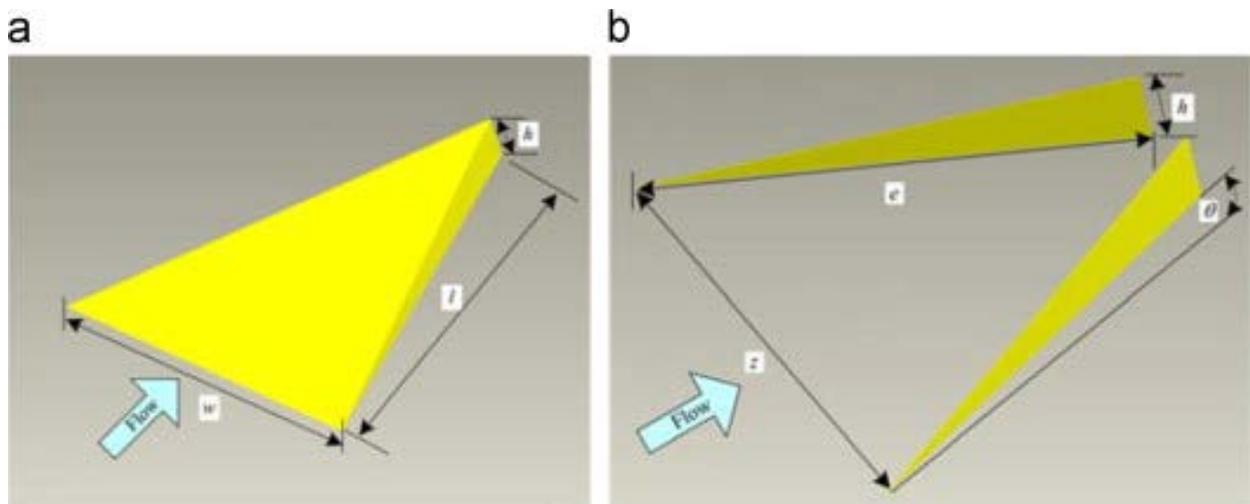
Figure 3 – Two prominent MVG geometries; (a) shows a ramp while (b) shows the vane model (Panaras & Lu, 2015).

With high velocities come compressibility effects; namely shock waves. Shock waves are an inevitable consequence of flying at speeds above Mach 1. As mentioned in the first section, much research is being done to try and reduce the negative effects of these shock waves as much as possible. MVGs are one control design that may be able to alleviate some of these negative consequences.

The main area of focus for applying these MVGs is for airfoils experiencing transonic flow and for engine inlets. As shocks in transonic flow only happen at particular conditions, engine inlets have been more widely studied and are therefore the focus of this report. Titchener and Babinsky (2015) have done a generous amount of research on the subject and a summary of past research is presented in the appendix for the reader. The summary is well done and highly recommended for anyone interested in the subject at hand.

Before investigating how MVGs affect flow through a shock wave, it is important to first understand what happens upstream of the shock wave. Although the geometry of the ramp MVG appears rather simple, the flow pattern it creates is quite complex. Several independent vortices are created from a single point that interact with each other and the surface of the underlying plane.

Figure 4 shows a Large Eddy Simulation (LES) that details some of these vortices. There is a major, outer, vortex that forms that encompasses one or two minor vortices in the middle, depending on the type of MVG used (Lu, Pierce, & Shih, 2010). The schlieren snapshot shows a side view of these vortices along with the shockwaves that form from the MVG itself. These shockwaves also interact with the trailing vortices but will not be discussed in depth in this report. A top view of an experiment with a ramp MVG is shown in Figure 5 for an additional reference that points out the primary and secondary vortices.

Now to combine the MVG with the shock wave. Again, Titchener and Babinsky (2013) studied the effects of MVGs on a normal shock wave, as might be experienced at an engine inlet. Their studies showed that MVGs are effective in reducing the flow separation after the normal shock as well as reducing the unsteadiness of the shock wave itself (Titchener & Babinsky, 2013). Schlieren images of their findings are presented in Figure 6.
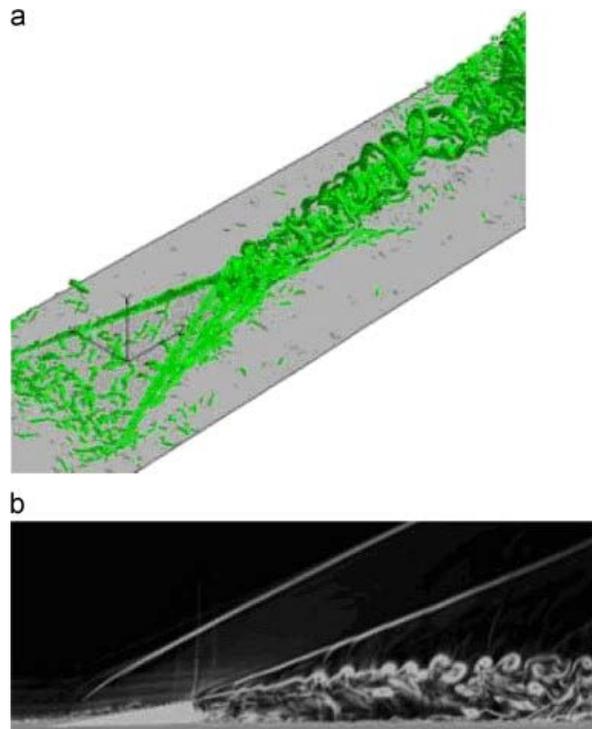
Figure 4 – (a) View of CFD simulation showing vortices and (b) side schlieren view (Lu et al., 2010).
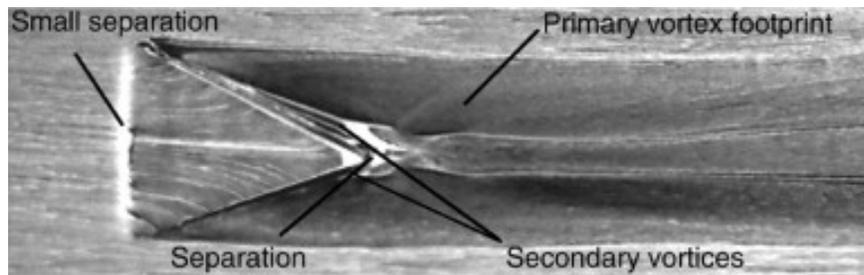
Figure 5 – Top view of a ramp MVG in supersonic flow with features detailed (Babinsky, Li, & Pitt Ford, 2009).
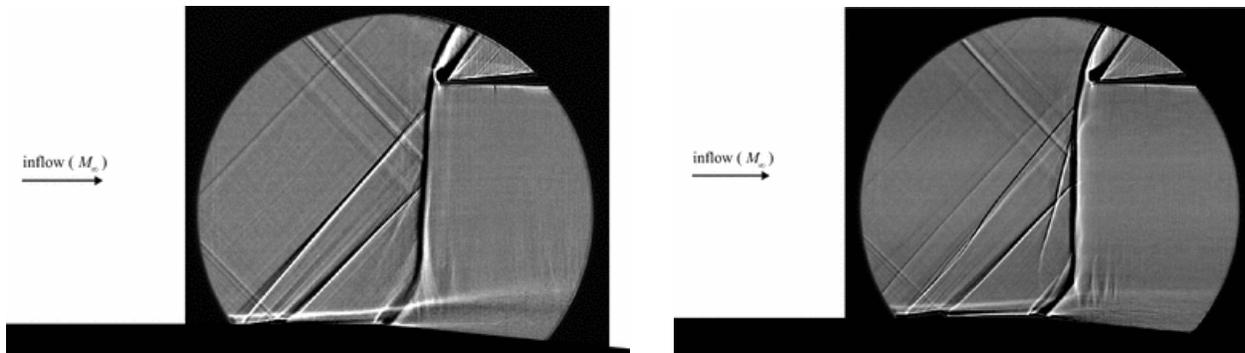
Figure 6 – Schlieren images of a normal shock wave with (left) and without (right) an MVG upstream (Titchener & Babinsky,

2013).

Babinsky is not the only one to investigate these effects, however. Troia, Patel, Crouse, & Hall (2011) also studied MVGs on normal shocks via CFD. They obtained similar results to those of Babinsky although the simulations were run at different Mach numbers. Their results can be seen in Figure 7. Wang, Liu, Zhao, Fan, & Wang (2012) also conducted similar research and their results can clearly show the reduction in the boundary layer thanks to the placement of an MVG (not visible in the image).
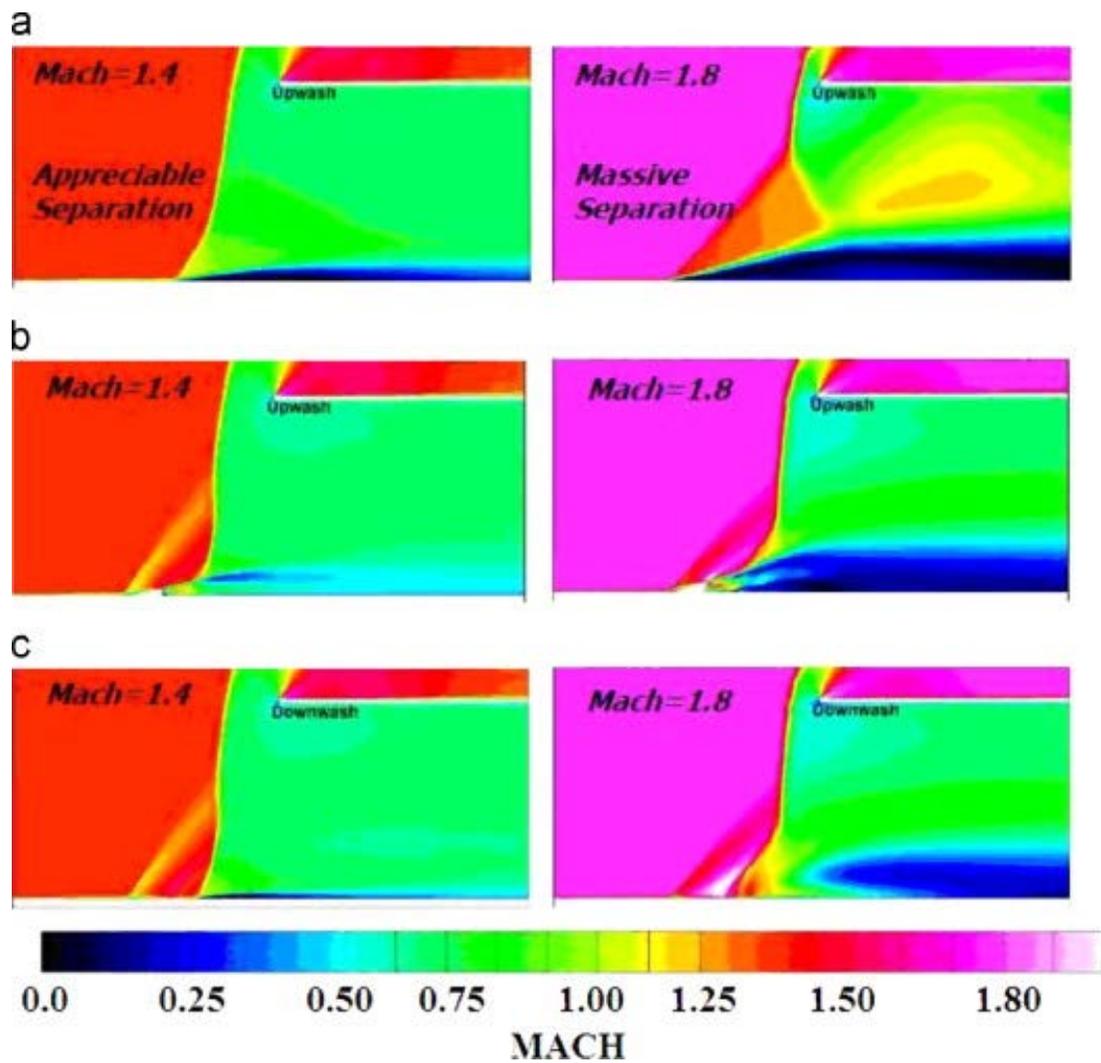
Figure 7 – CFD results of normal shockwave at an inlet for M = 1.4 and 1.8 (Troia et al., 2010).
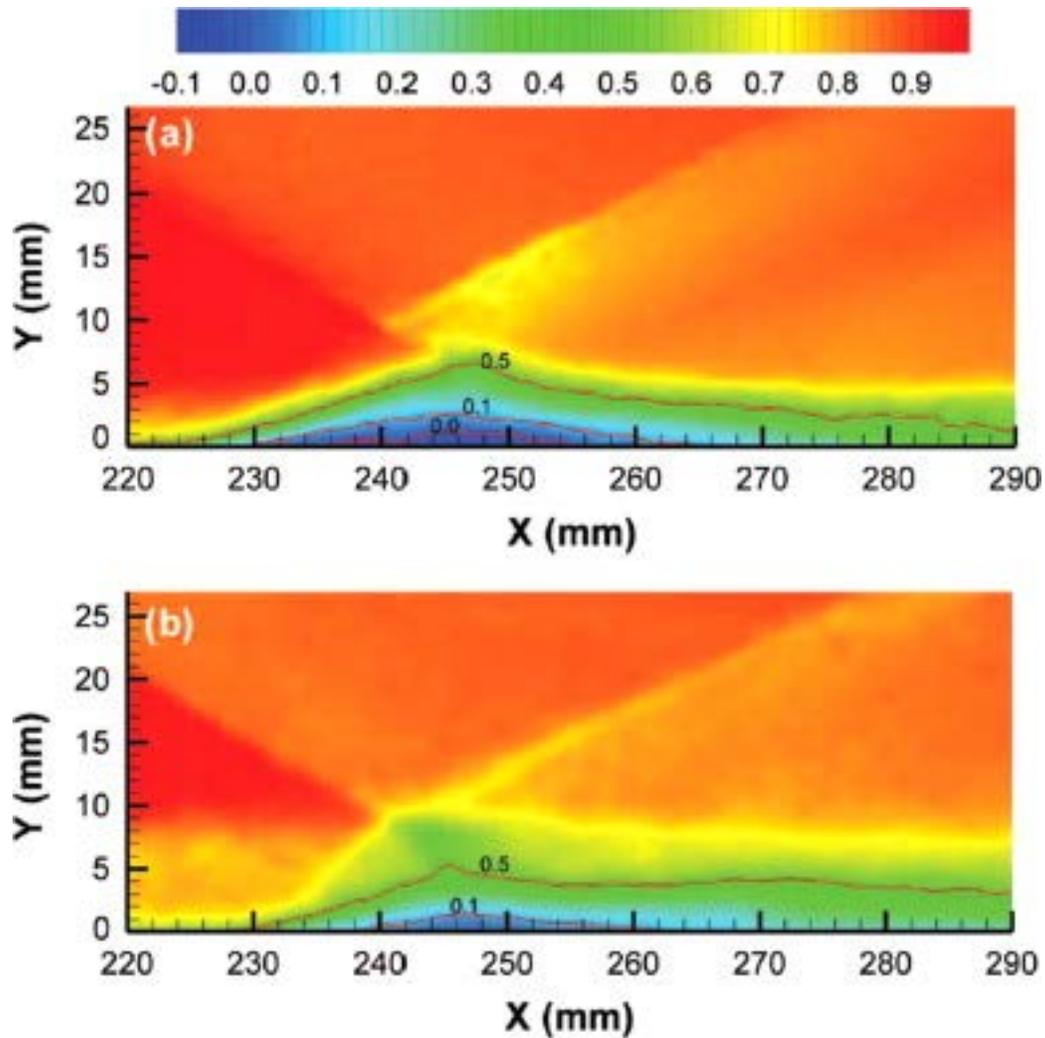
Figure 8 – Results from Wang et al. (2012) show flow without an MVG (top) and flow with an MVG (bottom). The MVG is ahead

of the flow and not shown in these images.

As opposed to the normal shock experiments of Troia et al. (2010), oblique shock waves

are also of concern and have been studied by many. The method for doing so is to simply place

an MVG in front of an inclined ramp. This generates an oblique shock wave if the flow

conditions are correct. The MVG has a similar effect as it did for the normal shockwave where

vortices are generated that delay flow separation and even decrease the power of the shock itself.

A schlieren image provided by Li and Liu (2011) is shown in Figure 9.
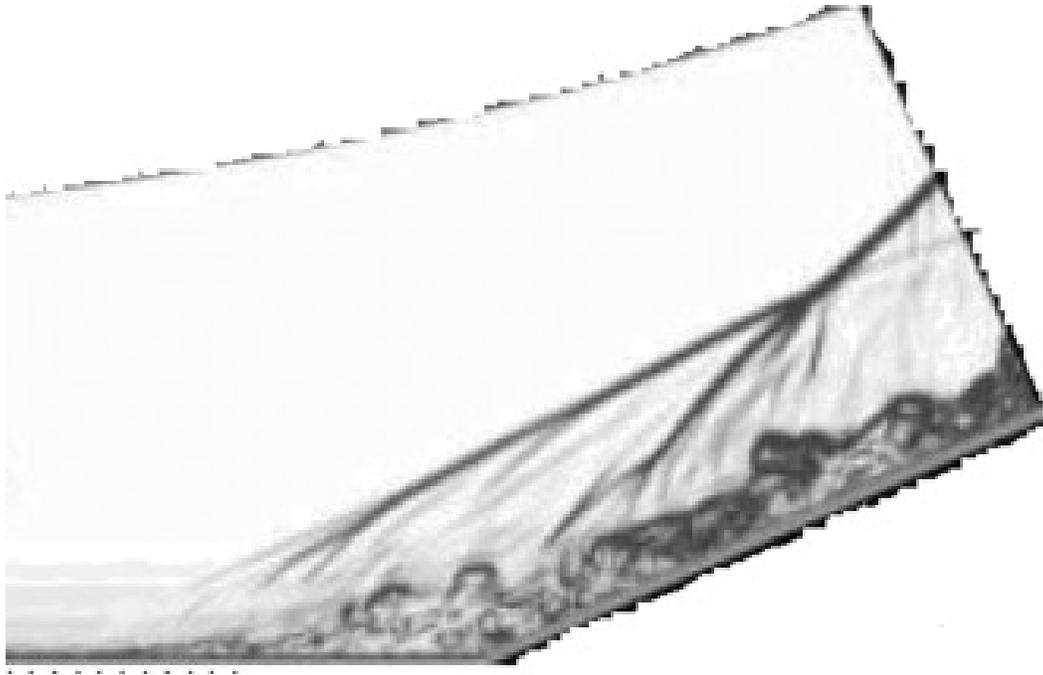
Figure 9 – Schlieren of ramp induced shock waves (Li & Liu, 2011).

So far, all of the MVGs that have been mentioned are categorized as being "passive", meaning they are an inherent part of the design and do not move. It has been noted that the ability to control the MVGs would be beneficial and that is indeed true. Being able to retract the MVGs during flight conditions when no shockwaves are present is an obvious advantage as otherwise the MVGs become ineffective and only increase the drag. While there is potential for these devices, further research needs to be conducted in order to affirm the overall worth of these kinds of MVGs.

This report will follow the basic setup as described by Yan et al. (2017) to investigate the effects of an MVG on an oblique shock generated by a ramp. The dimensions for the simulation are given in Figure 10. As described in the first section, the experimental team ran the tests based on the assumption of an optimal height. The summary by Titchener and Babinsky (2013) reveals that different tests have been run at varying heights with equally varying results. This is shown in Figure 11. While Yan et al. (2017) used a height of 50% of the boundary layer height for their

MVG, recent research by Martis and Misra (2013) has shown that a height of 70% is optimal for

their given conditions. This variance in MVG heights and their results has led to the main

purpose of this project.

1.3 PROJECT PROPOSAL

        The purpose of this project is to optimize the height of a ramp micro vortex generator as

described by Yan et al. (2017) to minimize the flow separation after the shock boundary layer

interactions. The given conditions are M = 2.5 and Re = 5760. Both RANS and LES simulations

will be run and compared as both methods have strengths and weaknesses pertaining to the

boundary layer and the flow field in general.
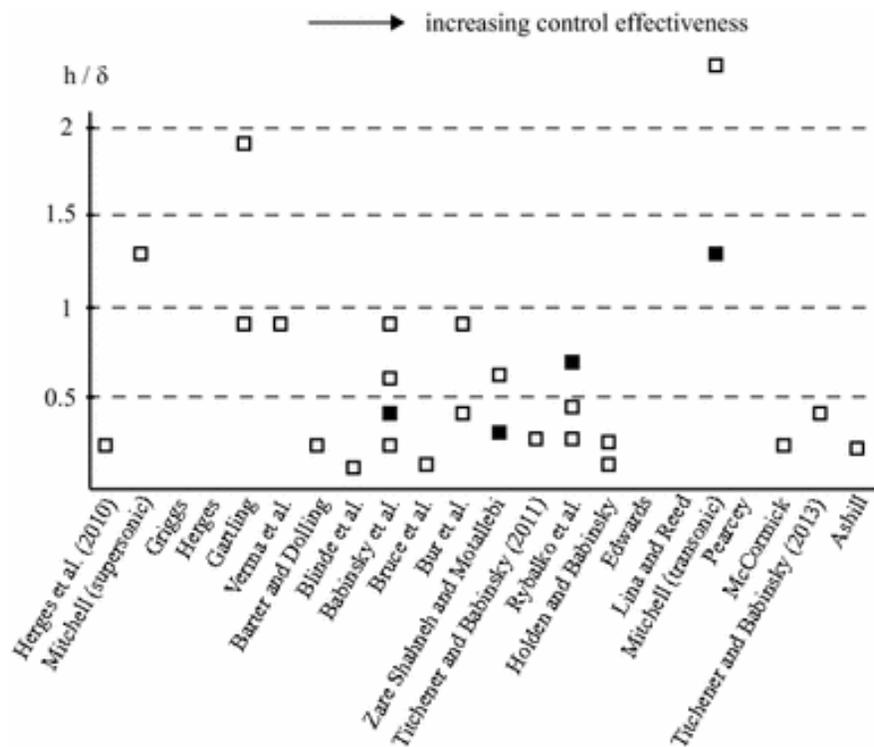
Figure 10 – Survey of ratios of height over boundary layer thickness for previously tested MVGs (Titchener & Babinsky, 2015.)
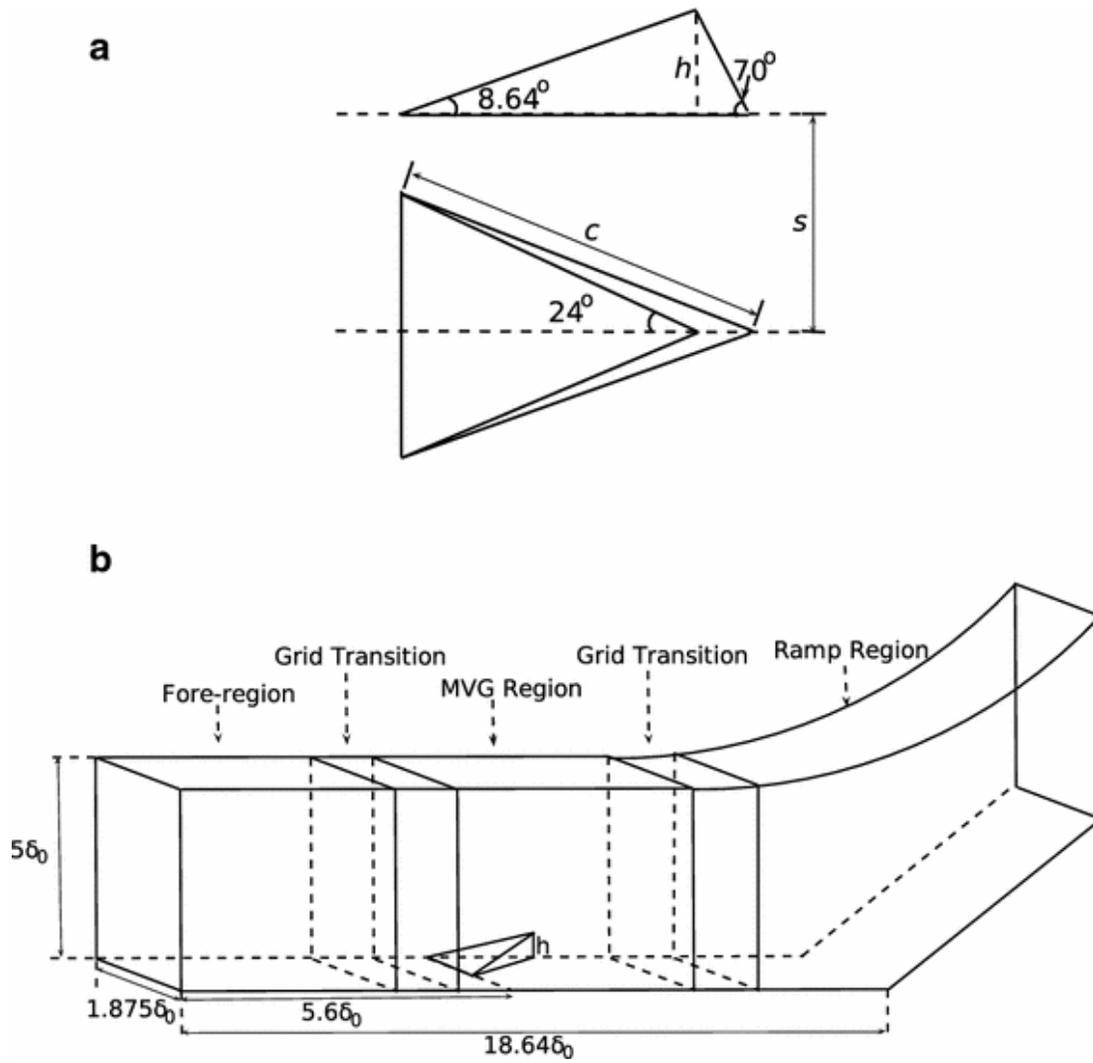
*Figure 11 – Geometrical dimensions (a) of the MVG and (b) of the experimental setup by Yan et al. (2017).*

Mathematical Equations and Assumptions

2.1 MATHEMATICAL EQUATIONS

Ansys Fluent is a CFD program that, like other CFD programs, allows the user to set up a geometrical domain, give environmental or boundary conditions and solve for the theoretical flow based on a series of numerical analyses. For one unfamiliar with aerodynamics or CFD this might seem like a simple and straightforward process. However, there is currently no mathematical way to solve for an entire flow field as a whole. In other words, there is no single equation that can give all the flow properties of a fluid that takes the geometry and other factors into account. Instead, what CFD and other finite element analysis (FEA) software does is divide the geometry into many subsections called cells with points called nodes at the corner of each cell. Rather than solving for an area or volume as a whole, each node is solved individually. When these nodes are looked at collectively, a general pattern of the flow can be obtained.

Additionally, as stated before, there is not a single equation solved at each of these points but a series of equations that are solved, allowing for all of the flow properties to be calculated. These equations are known as the Navier-Stokes equations (equations 1-5), named after the two men who each independently developed them in the early 1800's (Anderson, 2001).

2.1.1 Navier-Stokes Equations

The Navier-Stokes equations are broken up into three main categories: continuity, momentum, and energy. This is due to their derivations from three fundamental laws of nature; namely that mass, momentum and energy within a defined space are all conserved. While the full derivations of these equations will not be explained in this report, a brief description is provided for the reader.

Continuity:

$$\frac{\partial \rho}{\partial t} = -\left[\frac{\partial(\rho u)}{\partial x} + \frac{\partial(\rho v)}{\partial y} + \frac{\partial(\rho w)}{\partial z}\right] \tag{1}$$

x momentum:

$$\frac{\partial u}{\partial t} = -u\frac{\partial u}{\partial x} - v\frac{\partial u}{\partial y} - w\frac{\partial u}{\partial z} + \frac{1}{\rho}\left[-\frac{\partial p}{\partial x} + \frac{\partial \tau_{xx}}{\partial x} + \frac{\partial \tau_{yx}}{\partial y} + \frac{\partial \tau_{zx}}{\partial z}\right] \tag{2}$$

y momentum:

$$\frac{\partial v}{\partial t} = -u\frac{\partial v}{\partial x} - v\frac{\partial v}{\partial y} - w\frac{\partial v}{\partial z} + \frac{1}{\rho}\left[-\frac{\partial p}{\partial y} + \frac{\partial \tau_{xy}}{\partial x} + \frac{\partial \tau_{yy}}{\partial y} + \frac{\partial \tau_{zy}}{\partial z}\right] \tag{3}$$

z momentum:

$$\frac{\partial w}{\partial t} = -u\frac{\partial w}{\partial x} - v\frac{\partial w}{\partial y} - w\frac{\partial w}{\partial z} + \frac{1}{\rho}\left[-\frac{\partial p}{\partial z} + \frac{\partial \tau_{xz}}{\partial x} + \frac{\partial \tau_{yz}}{\partial y} + \frac{\partial \tau_{zz}}{\partial z}\right] \tag{4}$$

Energy:

$$\frac{\partial(e + V^2/2)}{\partial t} = -u\frac{\partial(e + V^2/2)}{\partial x} - v\frac{\partial(e + V^2/2)}{\partial y} - w\frac{\partial(e + V^2/2)}{\partial z} + \dot{q} \tag{5}$$

$$+ \frac{1}{\rho}\left[\frac{\partial}{\partial x}\left(k\frac{\partial T}{\partial x}\right) + \frac{\partial}{\partial y}\left(k\frac{\partial T}{\partial y}\right) + \frac{\partial}{\partial z}\left(k\frac{\partial T}{\partial z}\right)\right.$$

$$- \frac{\partial(pu)}{\partial x} - \frac{\partial(pv)}{\partial y} - \frac{\partial(pw)}{\partial z} + \frac{\partial(u\tau_{xx})}{\partial x} + \frac{\partial(u\tau_{yx})}{\partial y}$$

$$+ \frac{\partial(u\tau_{zx})}{\partial z} + \frac{\partial(v\tau_{xy})}{\partial x} + \frac{\partial(v\tau_{yy})}{\partial y} + \frac{\partial(v\tau_{zy})}{\partial z} + \frac{\partial(w\tau_{xz})}{\partial x}$$

$$+ \left.\frac{\partial(w\tau_{yz})}{\partial y} + \frac{\partial(w\tau_{zz})}{\partial z}\right]$$

No matter what the control volume is, matter itself is conserved within it; meaning that mass is neither created or destroyed within the volume. Therefore, everything that goes into the volume either comes out of it or affects the density of the volume. If the right-hand side of equation 1 were added to the other side, it is easier to see that the net flux of these inputs, outputs, and changes in each direction negate each other, resulting in a sum total of zero.

The momentum equations are based off of Newton's second law of motion. This law states that the force of an object is equal to its mass multiplied by its acceleration. If, instead of looking at a control volume, we look at a single particle, the forces acting on it can be described

as in Figure 12. By summing the forces applied in each direction, the net force for each direction

is calculated. By applying these forces to Newton's law, the three equations for momentum are

obtained. Once again, if the right-hand side of these equations are added to the other, it is easy to

see that all changes of the momentum result in a net flux value of zero.
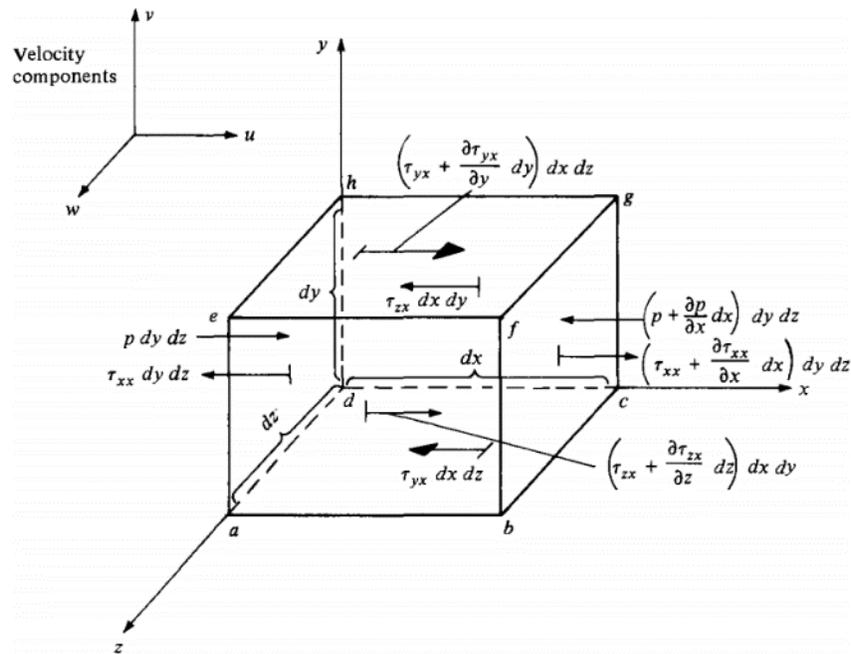
Figure 12 – Shear and other forces acting on a fluid element which constitute the momentum equations (Anderson, 2001).

The momentum equations first shown are simplified, partially for space considerations.

However, the full equations where the shear terms have been expanded are provided below.

These are the full momentum equations for three-dimensional, viscous, unsteady, and

compressible flow and are included because the simulations being performed fall into each of

those categories. Each variable needs to be taken into consideration when attempting to calculate

an accurate answer.

$$\rho\frac{\partial u}{\partial t} + \rho u\frac{\partial u}{\partial x} + \rho v\frac{\partial u}{\partial y} + \rho w\frac{\partial u}{\partial z} = -\frac{\partial p}{\partial x} + \frac{\partial}{\partial x}\left(\lambda\nabla\cdot\mathbf{V} + 2\mu\frac{\partial u}{\partial x}\right) \tag{6}$$
$$+ \frac{\partial}{\partial y}\left[\mu\left(\frac{\partial v}{\partial x} + \frac{\partial u}{\partial y}\right)\right] + \frac{\partial}{\partial z}\left[\mu\left(\frac{\partial u}{\partial z} + \frac{\partial w}{\partial x}\right)\right]$$

$$\rho\frac{\partial v}{\partial t} + \rho u\frac{\partial v}{\partial x} + \rho v\frac{\partial v}{\partial y} + \rho w\frac{\partial v}{\partial z} = -\frac{\partial p}{\partial y} + \frac{\partial}{\partial x}\left[\mu\left(\frac{\partial v}{\partial x} + \frac{\partial u}{\partial y}\right)\right] \tag{7}$$

$$+ \frac{\partial}{\partial y}\left(\lambda\nabla\cdot\mathbf{V} + 2\mu\frac{\partial v}{\partial y}\right) + \frac{\partial}{\partial z}\left[\mu\left(\frac{\partial w}{\partial y} + \frac{\partial v}{\partial z}\right)\right]$$

$$\rho\frac{\partial w}{\partial t} + \rho u\frac{\partial w}{\partial x} + \rho v\frac{\partial w}{\partial y} + \rho w\frac{\partial w}{\partial z} = -\frac{\partial p}{\partial z} + \frac{\partial}{\partial x}\left[\mu\left(\frac{\partial u}{\partial z} + \frac{\partial w}{\partial x}\right)\right] \tag{8}$$

$$+ \frac{\partial}{\partial y}\left[\mu\left(\frac{\partial w}{\partial y} + \frac{\partial v}{\partial z}\right)\right] + \frac{\partial}{\partial z}\left(\lambda\nabla\cdot\mathbf{V} + 2\mu\frac{\partial w}{\partial z}\right)$$

The energy equation is the last of the Navier-Stokes equations and accounts for the

energy and heat involved in the system. This equation is also rather long as it not only includes

the heat that enters and leaves the fluid particle but it also includes the work done by and/or on

the particle. These influences are shown in Figure 13. Similar to the previous equations, when

the forces are added together in their respective directions, the energy equation results. In

simulations where heat transfer is not a prominent contributing factor, the equation gets reduced

significantly to the point that the energy equation is de-coupled from the others. As this

experiment neglects heat transfer, the equation is greatly simplified and makes the equations

much easier to solve.
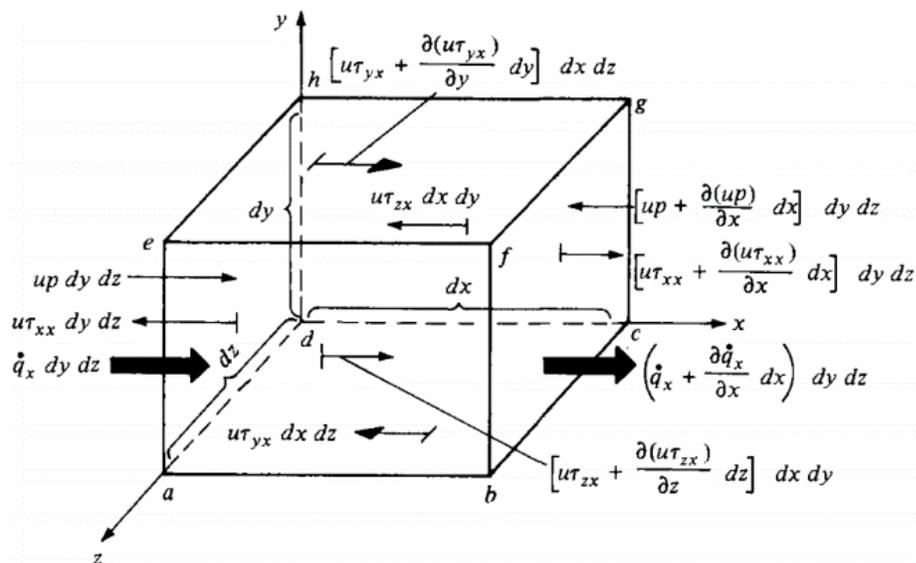
*Figure 13 – Heat transfer and other forces acting on fluid element which constitute the energy equation (Anderson, 2001).*

2.1.2 Nondimensional Parameters

The Navier-Stokes equations are crucial for solving any theoretical flow scenario and are the "back bone" for obtaining the necessary properties. There are other equations and parameters, though, that are necessary for matching flow conditions and ensuring the simulations are comparable.

The two main nondimensional parameters are the Mach number (Ma) and the Reynold's number (Re). The equations for these are shown below. The Mach number is a measurement of how fast a fluid is moving compared to the speed of sound in the medium. This setup has a Mach number of 2.5 meaning the flow is moving more than twice the speed of sound of the air.

$$Ma = \frac{U}{a} \hspace{4cm} (9)$$

$$Re_x = \frac{\rho \cdot U \cdot x}{\mu} \hspace{4cm} (10)$$

The Reynold's number compares inertial forces to viscous forces; or in other words, the momentum of a fluid to its internal, frictional forces. The Reynold's number also determines what type of flow occurs; either laminar, turbulent or transitory. The type of flow affects which equations are used to determine shear on the surface, boundary layer growth, and which type of solver is needed for accurate results when using CFD software. As the boundary layer is a vital component of the simulation, the Reynold's number needs to be the same in order to achieve comparable results.

Other nondimensional parameters, such as the Prandtl number and Knudsen number, will not be defined here. While they technically play a part in the analysis, their roles are comparatively minor and therefore are only mentioned so as to assure the reader that they have been considered.

2.1.3 Boundary Layer Equations

Analyzing boundary layers and representing them in a mathematical manner can be one

of the most complex tasks in aerodynamics. Yet, for many aerodynamic problems, including this

project, the boundary layer (BL) is a prominent feature. Fortunately, by nondimensionalizing the

Navier-Stokes equations and making a few assumptions, equations for this type of flow can be

obtained. Once again, the derivation will not be presented but the resulting equations are shown

below. These are applicable for 2D situations.

$$\text{Continuity:} \quad \frac{\partial(\rho u)}{\partial x} + \frac{\partial(\rho v)}{\partial y} = 0 \tag{11}$$

$$\text{x momentum:} \quad \rho u \frac{\partial u}{\partial x} + \rho v \frac{\partial u}{\partial y} = -\frac{dp_e}{dx} + \frac{\partial}{\partial y}\left(\mu \frac{\partial u}{\partial y}\right) \tag{12}$$

$$\text{y momentum:} \quad \frac{\partial p}{\partial y} = 0 \tag{13}$$

$$\text{Energy:} \quad \rho u \frac{\partial h}{\partial x} + \rho v \frac{\partial h}{\partial y} = \frac{\partial}{\partial y}\left(k \frac{\partial T}{\partial y}\right) + u \frac{dp_e}{dx} + \mu \left(\frac{\partial u}{\partial y}\right)^2 \tag{14}$$

Vital equations describing the displacement thickness and momentum thickness of the

boundary layer are also given by Anderson (2001).

$$\delta^* \equiv \int_0^{y_1} \left(1 - \frac{\rho u}{\rho_e u_e}\right) dy \quad \delta \leq y_1 \rightarrow \infty \tag{15}$$

$$\theta \equiv \int_0^{y_1} \frac{\rho u}{\rho_e u_e}\left(1 - \frac{u}{u_e}\right) dy \quad \delta \leq y_1 \rightarrow \infty \tag{16}$$

Past mathematicians and aerodynamicists have solved these equations for specific cases,

one of which was for a flat plate. As this experiment acts as a flat plate up until the MVG, these

equations should hold up to that point and have been used to assist with analysis. They are

known as the Blasius solutions. There are two sets, one for laminar flow and one for turbulent

flow. The equations for turbulent flow are shown as they will be used to calculate certain

dimensions (Cengel & Cimbala, n.d.).

$$\frac{\delta}{x} = \frac{.16}{\left(Re_x\right)^{\frac{1}{7}}} \tag{17}$$

$$\frac{\delta^*}{x} = \frac{.02}{\left(Re_x\right)^{\frac{1}{7}}} \tag{18}$$

$$\frac{\theta}{x} = \frac{.016}{\left(Re_x\right)^{\frac{1}{7}}} \tag{19}$$

2.1.4 Other Equations

There are multiple other equations that will are incorporated into the CFD solver which

need to be addressed. The ideal gas law will be used to add another equation to the Navier-

Stokes equations in an attempt to simplify and solve them. The isentropic flow equations will

also be used for hand calculations to verify results. These equations are given below (Anderson,

2001).

$$P = \rho RT \tag{20}$$

$$\frac{p_0}{p} = \left(1 + \frac{\gamma - 1}{2} M^2\right)^{\gamma/(\gamma-1)} \tag{21}$$

$$\frac{\rho_0}{\rho} = \left(1 + \frac{\gamma - 1}{2} M^2\right)^{1/(\gamma-1)} \tag{22}$$

2.2 ASSUMPTIONS

The Navier-Stokes equations are famous, if not infamous, for one main reason: they are

an unsolvable set of equations. There are more unknown variables than there are equations that

relate them, rendering them with an infinite number of solutions on their own. However, this does not deter engineers and mathematicians from utilizing them. By making certain assumptions, terms in the equations either become zero or are comparatively so small that they can be neglected. Other equations, likewise, have assumptions implicit with their use. The following is a list of those equations and the assumptions that need to be made in order to properly use them:

Navier-Stokes – Although many assumptions will be made later on which will simplify these equations, there is one main underlying condition that needs to be met. The medium in question needs to be considered a continuum in order for the Navier-Stokes equations to apply. This means that the particles in the fluid are close enough to each other that the fluid can be considered as such. The standard to determine this qualification is the Knudsen number which relates the distance between particles to an arbitrary length. If this value is much less than unity, the continuum assumption holds. The simulations for this project are performed at or near sea level conditions with compressibility effects considered. As such, the continuum assumption is acceptable.

Boundary Layer Equations – The boundary layer equations are based off one main assumption which is that the boundary layer height is much less than the reference length. If this relationship does not hold then previously ignored variables come into play and complicate the equations. There is also the implication that the Reynold's number is large while the Mach number is not inordinately large. As the Reynold's number describes inertial vs viscous forces, it makes sense that it needs to be high as otherwise the boundary layer would grow much more quickly. The limit on the Mach number is to keep heat transfer and other hypersonic concerns out of the analysis.

Another condition to note concerns boundary layer continuity. This refers to the change in pressure through the boundary layer. The assumption is that there is no change in pressure through the boundary layer (see equation 13); a concept that allows pitot tubes to function even though boundary layers develop.

Ideal Gas Law – The analyses performed uses and assumes that the fluid acts as an ideal gas. This implies that the ideal gas equation holds true, meaning that pressure, density, gas constant and temperature are related. This gives an extra equation which assists in solving the Navier-Stokes equations.

Isentropic Equations – All calculations and simulations are performed with the assumption that the processes are isentropic. Entropy is conserved, meaning that the processes are adiabatic and reversible. Even though the energy equation is included with the turbulence modeling, there is no heat transfer within the gas or to the surrounding walls.

Other assumptions are included to ensure that all aspects of the report are accounted for. As certain information was limited or as the analysis necessitated, assumptions about various aspects of the simulations had to be made. One such is described in the geometry section. The angle of the ramp is unknown and has been assumed to be 25 degrees. The exact values for the density, temperature and molecular weight are also assumed. As long as the Mach number and Reynold's number match, not knowing the exact values for these parameters should not change the outcome.

METHODOLOGY

ANSYS Fluent is the software employed to solve the problem at hand. The Workbench feature of ANSYS is used which encompasses everything from creating the initial geometry to visualizing the solution. The procedure follows the same basic steps as outlined below.

3.1 GEOMETRY

3.1.1 Presented Geometry

In order to compare results with those of Yan et al., the same general dimensions were used. These dimensions can be seen in Figure 10. An important detail to note is that most of the length dimensions are given with respect to δ which is the purported boundary length of the flow ahead of the MVG. In order to actually create the geometry, a value for this variable was needed. Therefore, this value was assumed to be the length variable used to calculate the Reynold's number. As the Reynold's number is known, δ was back-calculated and found to be approximately 0.001m (see section 3.1.2 for the calculation). With this variable defined, the rest of the dimensions were calculated.

Two of the geometries were not presented in the paper by Yan et al. These are the ramp angle and the radius of curvature above the ramp. While the radius of curvature likely does not affect the overall flow and can therefore be approximated, the ramp angle has a great potential to alter the results as this is directly correlated to the strength and angle of the shock wave. It is possible that these dimensions were given in the report cited by Yan et al. but unfortunately, access to this report was unavailable for comparison. As such, the ramp angle was estimated to be 25 degrees from the horizontal and this will be consistent for all of the simulations.

The purpose of this project is to test the effects of varying the height over boundary layer thickness ratio (h/δ). This is a geometrical factor and the ratios of 0.2 to 0.7 in intervals of 0.1

were tested. Cases with no MVG were included as an initial reference point for the data. This

gives a total of 14 simulations, 7 RANS and 7 LES. The geometry for a sample ratio of h/δ = 0.5

is shown in Figure 12.
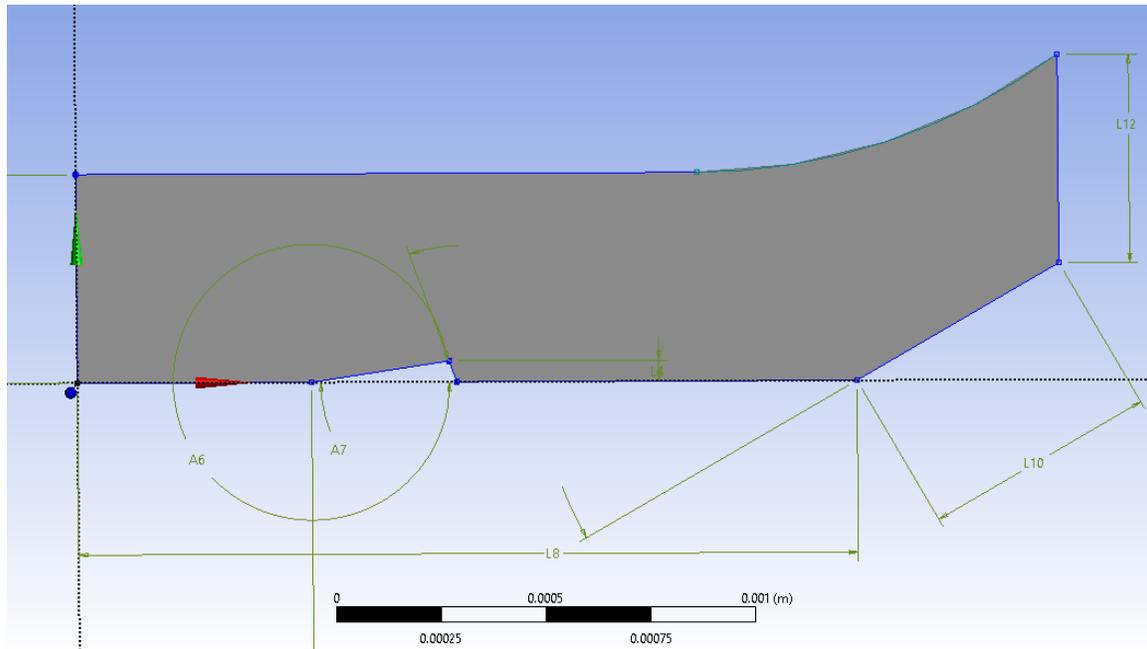
Figure 14 – The 2D geometry for the h/δ = 0.5 case.

3.1.2 Adapted Geometry

The above geometry is very similar to what was given in the work by Yan et al.

However, there is a small, yet important, detail concerning the Reynold's number used for the

simulations. The Reynold's number is based off of the momentum boundary layer thickness and

not based on a generic length. This necessitated that the geometry be altered in order to

accurately recreate what has previously been performed. A segment needed to be added in front

of the given geometry to allow the boundary layer to grow and attain the correct parameters.

Determining this new geometry required going through several calculations in order to find the

actual length of δ which is what all given dimensions are based on.

The process to find the value of δ starts with the given values of Mach and Reynold's number. From the definition of the Reynold's number, theta (θ) is derived. The Blasius solution for a turbulent momentum BL uses this value to solve for a given length x, which gives the necessary length needed for the BL to grow to such a height. A new δ is then calculated and the results are shown below.

Given Information:

$$Re_\theta = 5760 \qquad M = 2.5$$

$$Re_\theta = \frac{\rho \cdot V \cdot \theta}{\mu} \qquad M = \frac{V}{a} \qquad a = \sqrt{\gamma \cdot R \cdot T}$$

Assume gamma = 1.4   For air, $R = 287 \cdot \dfrac{J}{kg \cdot K}$

Values used in Ansys Fluent for ρ, μ and T:

$$\rho = 1.225 \cdot \frac{kg}{m^3} \qquad \mu = 1.7894 \cdot 10^{-5} \cdot \frac{kg}{m \cdot s} \qquad T = 288.16 \cdot K$$

Solve for the speed of sound:

$$a = \sqrt{\gamma \cdot R \cdot T} = \sqrt{1.4 \cdot 287 \cdot 288.16} = 340.3 \cdot \frac{m}{s} \qquad a = 340.3 \cdot \frac{m}{s}$$

Solve for Velocity:

$$M = \frac{V}{a} \qquad V = M \cdot a = 2.5 \cdot 340.3 = 850.67 \cdot \frac{m}{s} \qquad V = 850.67 \cdot \frac{m}{s}$$

Solve for θ:

$$Re_\theta = \frac{\rho \cdot V \cdot \theta}{\mu} \qquad \theta = \frac{Re_\theta \cdot \mu}{\rho \cdot V} = \frac{5760 \cdot 1.7894 \cdot 10^{-5}}{1.225 \cdot 850.67} = 9.8908 \cdot 10^{-5} \cdot m \qquad \theta = 9.8908 \cdot 10^{-5} \cdot m$$

Blasius solution for turbulent flow:

$$\theta = \frac{.016 \cdot x}{\left(\dfrac{\rho \cdot V \cdot x}{\mu}\right)^{\frac{1}{7}}} \qquad 9.8908 \cdot 10^{-5} = \frac{.016 \cdot x}{\left(\dfrac{1.225 \cdot 850.67 \cdot x}{1.7894 \cdot 10^{-5}}\right)^{\frac{1}{7}}}$$

Solving for x yields:

$$x = .0521389 m$$

This is the distance required to generate a BL with the appropriate momentum BL thickness. Now solve for δ to get the nominal BL thickness:

Blasius solution for δ:

$$\delta = \frac{.16 \cdot x}{\left(\frac{\rho \cdot V \cdot x}{\mu}\right)^{\frac{1}{7}}} \qquad \delta = \frac{.16 \cdot (.0521389)}{\left(\frac{1.225 \cdot 850.67 \cdot .0521389}{1.7894 \cdot 10^{-5}}\right)^{\frac{1}{7}}} = 9.8908 \cdot 10^{-4}$$

This makes sense as the equations for the two solutions only differ by a factor of 10.

With the x and δ value, the simulation can be properly sized.
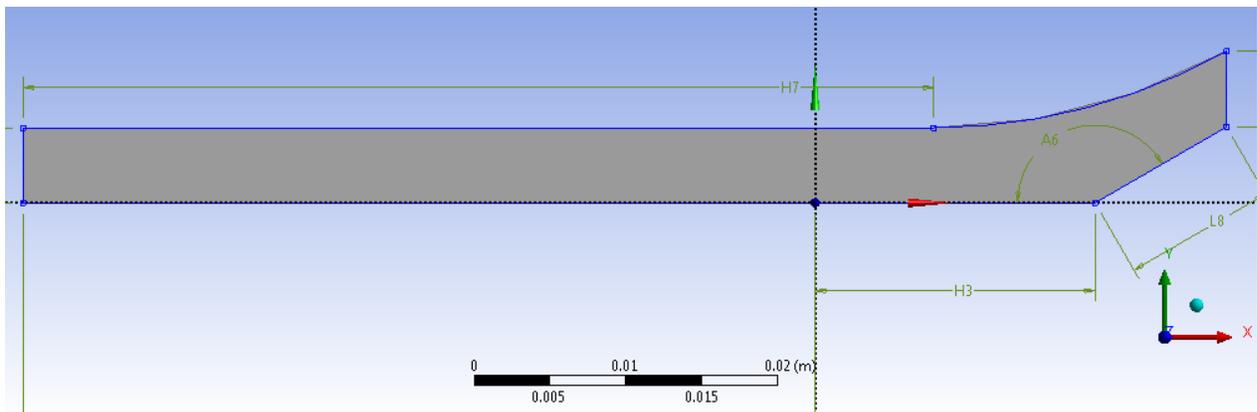
Figure 45 – The adapted geometry to ensure proper BL conditions.

To verify if the boundary layer height was correct, the front section was run through an incompressible case to match results of Yan et al. (2017). Velocity profile data was taken at the outlet of this case and the results are shown in Figure 16 and 17. As can be seen from Figure 17, the BL height does indeed reach the appropriate value at the right place, thereby confirming that the hand calculations are correct.
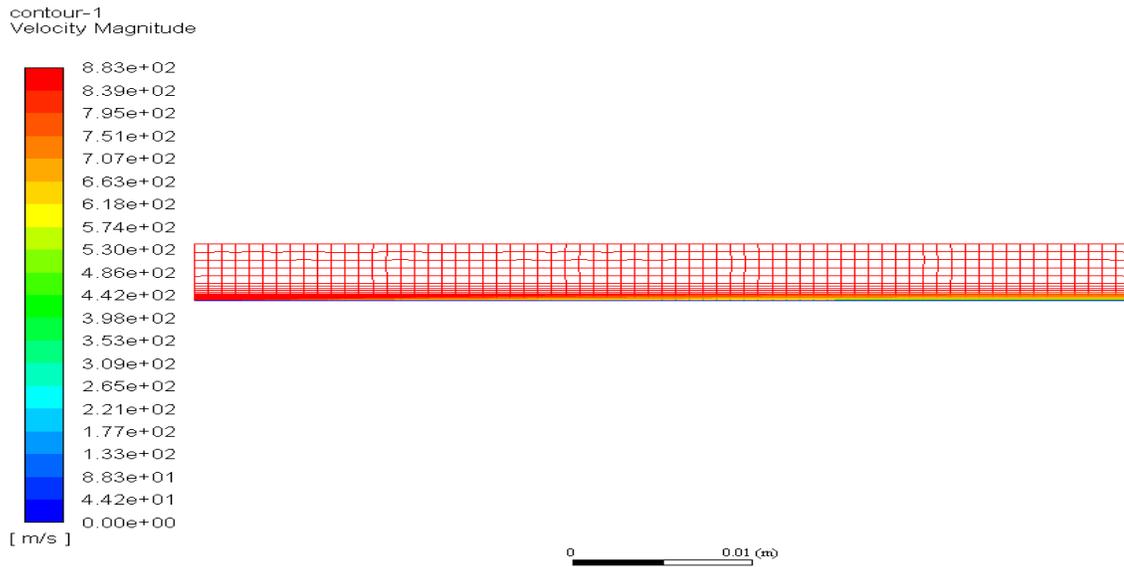
Figure 16 – Complete view of the added geometry section. A small BL can be seen at the lower right-hand side of the geometry.
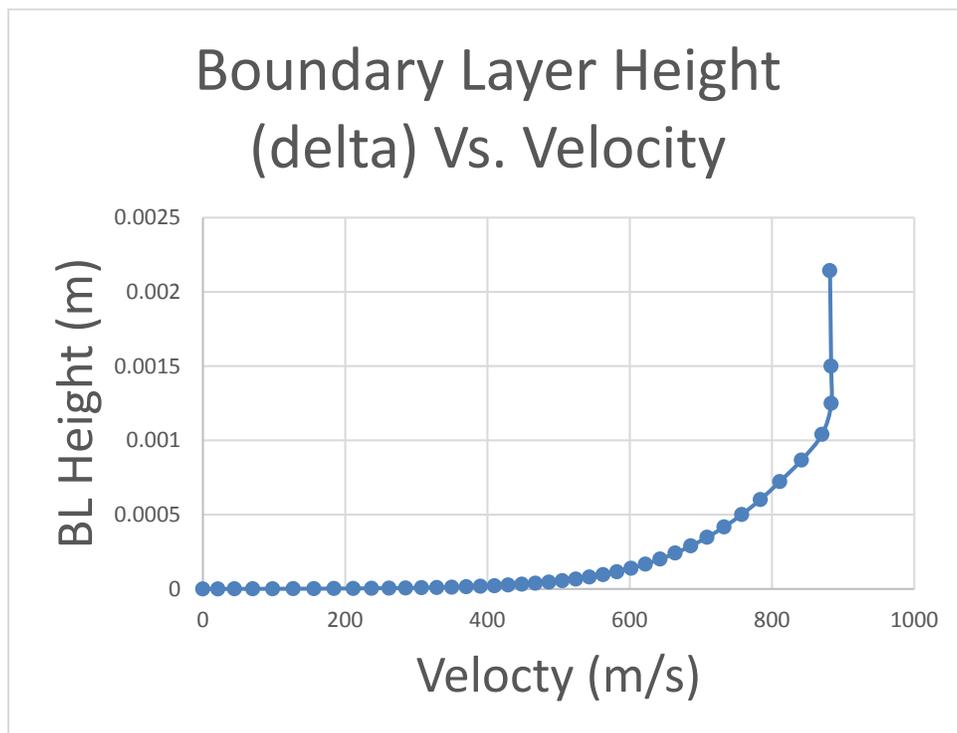

Figure 17 – The BL height vs the velocity taken at the end of the new geometry segment.

3.2 MESH GENERATION

3.2.1 2D Mesh Generation

A structured mesh was generated that followed the description shown in Figure 11. There is a large coarse region at the inlet, a fine region around the MVG and a transitional region before the fine region. There is no transitional region behind the MVG as the ramp region was deemed sufficiently fine to capture the flow physics. A bias was placed on the vertical sections, making the cell size larger the further it is from the bottom wall. The values for each section are given in the Table 1.

Table 1 – Values for the parameters of the 2D mesh.

| Location/Region	Number of Divisions	
Coarse		600
Transitional		100
Fine		230
Ramp		300
Vertical Walls		50
	Bias Growth Rate	1.2
Total Nodes		69972
Total Elements		68550
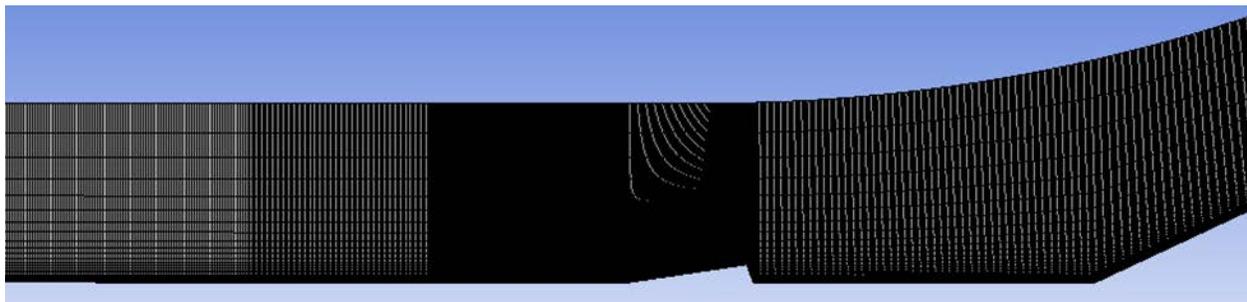
*Figure 18 – View of the overall mesh for the h/δ = 0.5 case.*
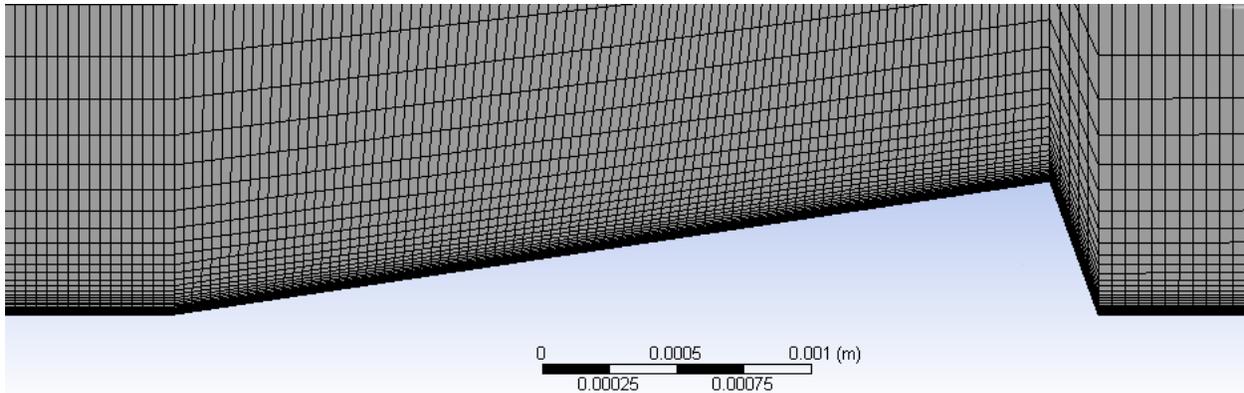
Figure 19 – A detailed view of the mesh showing the cell bias and structure around the MVG.

The wall spacing or cell size of the first cell next to a wall was calculated to properly

capture the boundary layer. As with any part of the mesh, if the cell size is too large, errors can

occur as the flow will not be well defined. The "y+" value is used to ensure that the mesh is

sufficiently fine to give accurate results. By using a y+ value of 1, a cell size of 3.135e-7 meters

was determined. With the boundary layer being a crucial part of the analysis, and as cell count

was not an issue for the 2D simulations, the wall spacing was closer to half that, or about 1.5e-7

meters. This was deemed small enough to properly capture the boundary layer with a small

margin of safety included.

3.2.2 3D Mesh Generation

The 3D mesh follows the same pattern as the 2D mesh. However, a feature of ANSYS

greatly impacted the mesh's layout. The maximum cell count of ANSYS is 512,000 elements.

The grid used in Yan et al.'s (2017) analyses had 39,321,600 elements; about 75 times more

elements than ANSYS would allow. If a decent solution is to be obtained using ANSYS,

elements would need to be used as efficiently as possible.

This fact affected every aspect of the grid. The divisions for almost every section

decreased. The coarse area and ramp area were reduced even further in an attempt to save

elements. To compensate for this, another transitional region behind the MVG was added,

making this setup split in the same manner as Figure 11. The new spanwise direction was also

not split into many divisions. The only aspect that remained about the same was the division

count along the vertical walls. The boundary layer needed to be properly captured, meaning the

count couldn't be reduced by much.
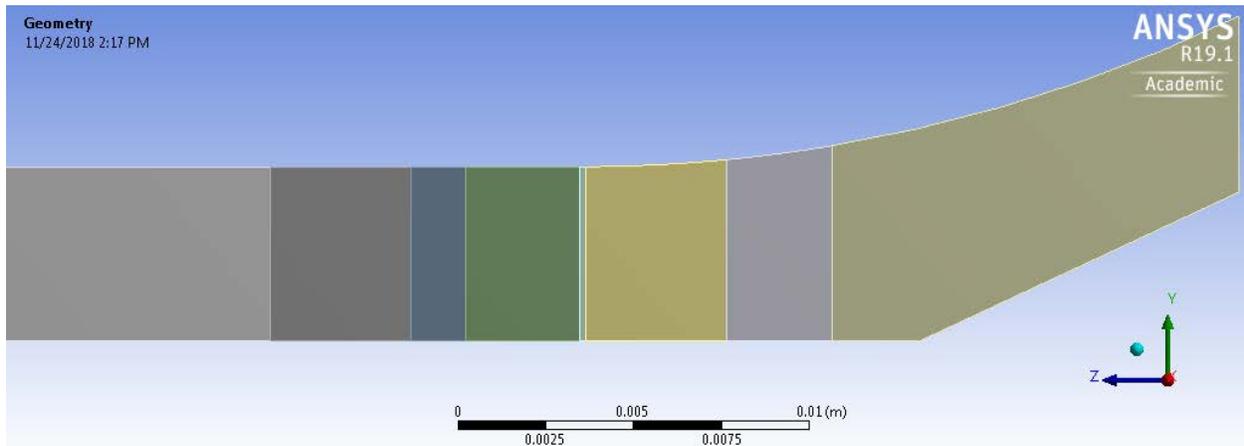
Figure 50 – Geometrical side view of the 3D simulation showing the different areas of mesh refinement.
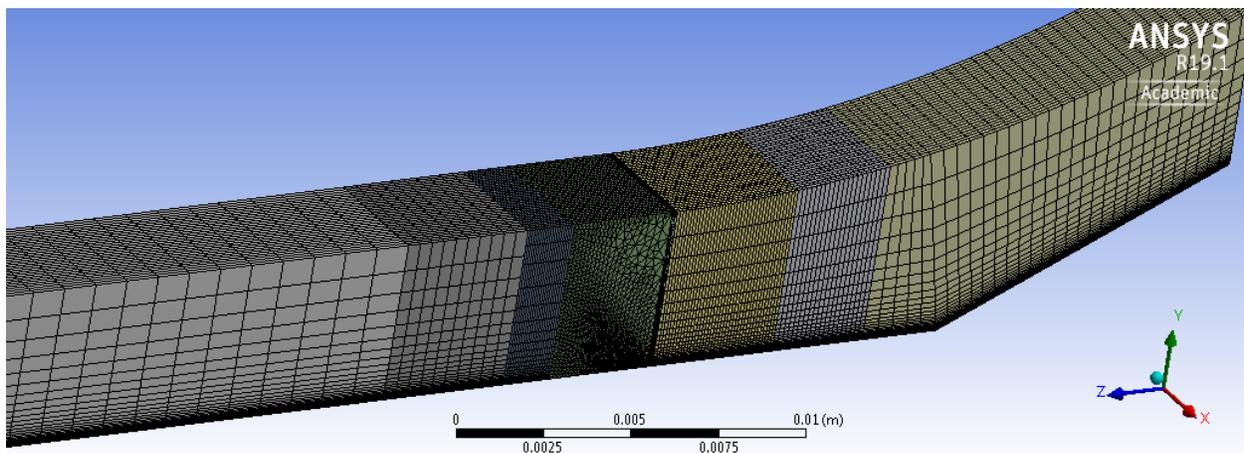

Figure 21 – Mesh view of the 3D simulation.

Another difficulty with ANSYS was its inability to create a structured mesh around the

MVG. Attempts were made to split the geometry around the MVG into rectangular sections

where a structured mesh could be generated. These attempts were unsuccessful as whichever

section contained the MVG geometry would not produce the desired structured mesh. In lieu of

this difficulty, a general size parameter was used for the section around the MVG. This explains

the drastic change in mesh composition as seen in Figure 22.
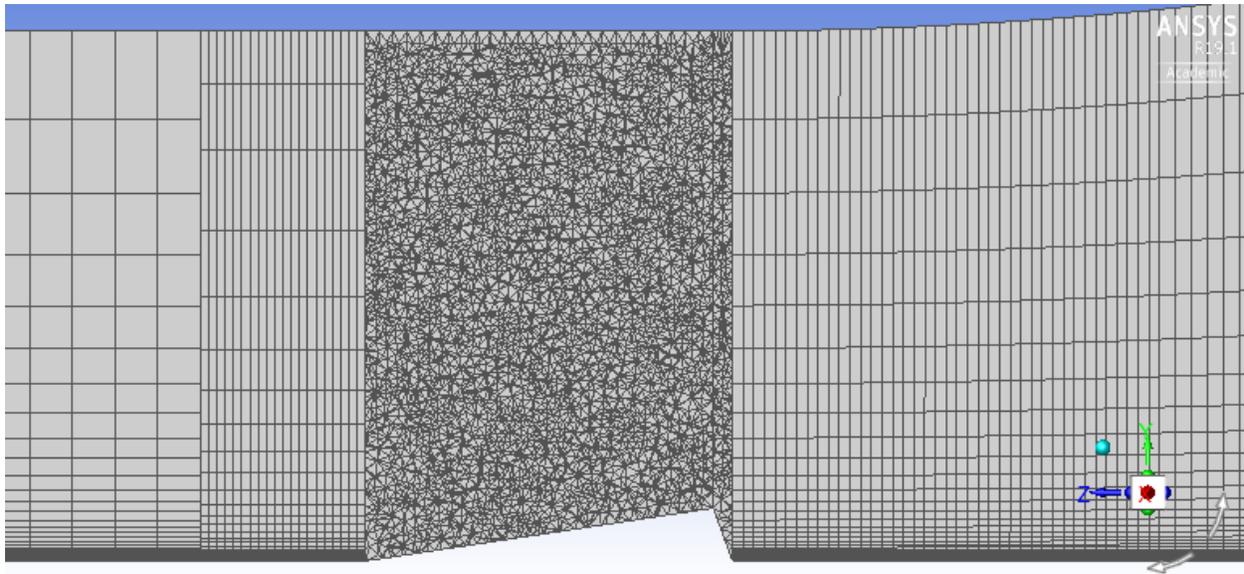
Figure 22 – Mid section mesh view of the 3D geometry detailing the area around the MVG.

3.3 MODELING

As is common with many CFD simulations, the flow goes from left to right. The left

boundary was designated as a velocity inlet, the top as a slip wall (no shear stress) and the right

side designated as a pressure outlet with extrapolated output. The bottom sides were considered

to be no-slip walls with a standard roughness setting applied. Standard temperature and dynamic

viscosity or air were used to determine that a velocity of 851 m/s was needed to match the Mach

number, as described in the adapted geometry section.

There are several methods that attempt to successfully model turbulent flows. One of

these methods uses the Reynolds-Averaged Navier-Stokes (RANS) equations. This method

introduces extra turbulence variables and equations to help close the solution. ANSYS Fluent offers three different sets of equations: Spalart-Allmaras, k-epsilon and k-omega.

The Spalart-Allmaras method was chosen as it only introduces one extra equation, thereby reducing the needed computational time. It is also good for low Reynold's number flows and where the boundary layer experiences adverse pressure gradients. It is not recommended to use the model for predicting turbulent decay, which is partly why the LES model is used in tandem with the RANS simulations to represent the flow (Reynolds Averaged…, 2009).

The Large Eddy Simulation (LES) attempts to model turbulence in a different manner. In addition to adding extra variables, a filter is introduced with the Navier-Stokes equations where any eddies smaller than a certain size (normally the cell size) are ignored. However, the larger eddies that remain are modeled using the full Navier-Stokes equations. This typically requires greater computational time or power as a higher order spatial discretization is needed (Reynolds Averaged…, 2009).

The simulation was density based as opposed to pressure based to stay consistent with previous research. Either the Spalart-Allmaras or LES models were used to determine the flow, as discussed. The air was considered to be an ideal gas with default properties for specific heat, thermal conductivity, viscosity and molecular weight. The gradient for the spatial discretization was least squares cell based with the modified turbulent viscosity method being a first order upwind schema. The transient formulation was first order for the Spalart-Allmaras simulations and second order for the LES simulations. A time step of 0.0005 seconds with 20-25 intermediate iterations were used for each LES case. A hybrid initialization with 20 iterations was also used to give a better starting point for the solution.

3.4 GRID CONVERGENCE STUDY

A grid convergence study was performed to ensure that the solutions were grid independent. One method of determining grid independence is to compare an inviscid simulation with its viscous counterpart. This type of study was not done as the boundary layer plays a critical role in the analysis and therefore, an inviscid solution would have relatively little meaning. Instead, the same viscous simulation was run with an increasing number of nodes and the results were compared. The low, medium and high values represent the level of grid refinement with 57400, 63,000 and 68550 elements each, respectively.

The graph below shows the velocity profile results at the ramp corner for the RANS $h/\delta = 0.5$ case. The different levels agree very well with a little divergence from the medium case. The medium case was run for a few hundred iterations less than the others. This difference in convergence is suspected to be the cause of the divergence and not the refinement of the grid.

A similar number of nodes was used for the LES cases. The residuals of the LES simulations did not converge as well as those of the RANS simulations (some variables oscillated much more), making their results more difficult to compare. However, the high cell count of the simulations and the low-to-zero variability of the RANS grid results suggest that whatever error may be present will be low. The LES simulations were run with the highest cell count as another safety factor.
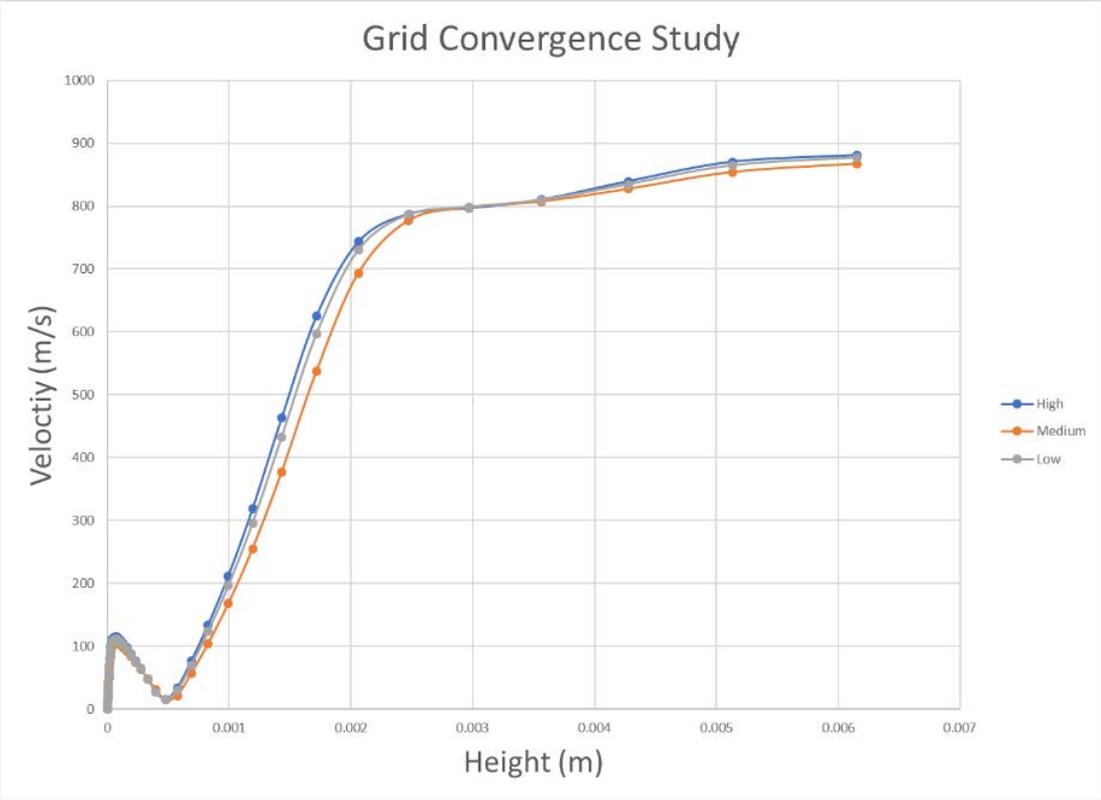
Figure 23 – The grid convergence study for the 2D RANS case.

RESULTS

4.1 2D RESULTS

The RANS simulations were run for 5,000+ global iterations. The LES simulations were

generally run for 10,000+ iterations using the RANS solution as a starting point. This was to help

the LES simulations converge. For almost every case that was solved entirely using the LES

method, the boundary layer grew and shrunk as opposed to steadily increasing in size. This flow

pattern did not disappear with continuing iterations and kept the simulation from converging. An

example of this large flux can be seen in Figure 24. Even with the RANS solution initialization,

the LES simulations never converged as well as the RANS simulations. The LES simulations

were considered converged after similar oscillations were observed over thousands of iterations.
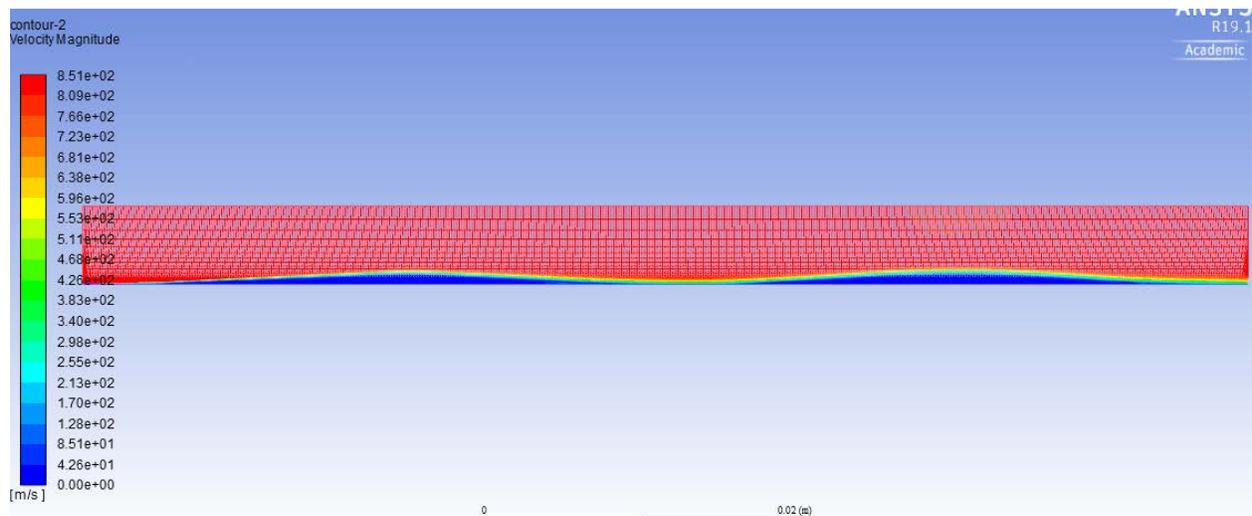
Figure 24 - LES simulation of a simple tube showing the uneven BL generated.

The pressure and velocity contours for each simulation were recorded; however, only a

sample of these are given in the report for reference. The entirety of these contour plots is found

in Appendix B – Pressure and velocity contours.

Velocity at three locations within the geometry were plotted for each simulation. These

locations occur after the MVG but before the ramp, at the ramp corner, and halfway up the ramp,

perpendicular to the wall. These locations, which will be referred to as planes, are seen in Figure

27. The legend values for each plot refer to the height of the MVG. In addition, velocity data was

taken at the original inlet (before the geometry was augmented) to verify that the boundary layer

height was indeed what it should be for each simulation.
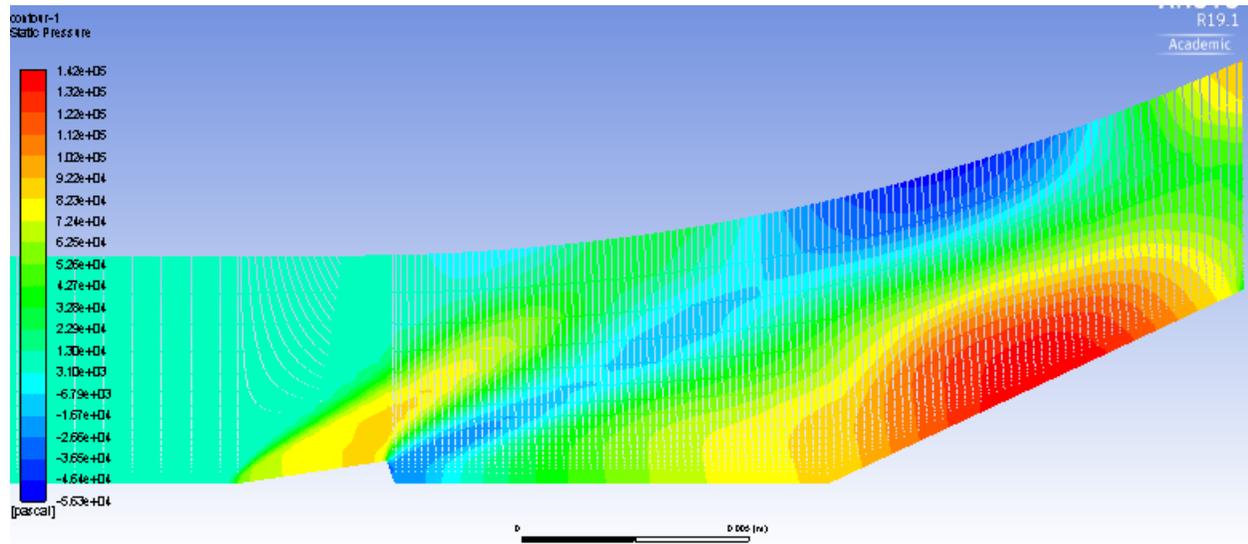
*Figure 25 – Sample pressure contour plot of the RANS 0.5 case.*
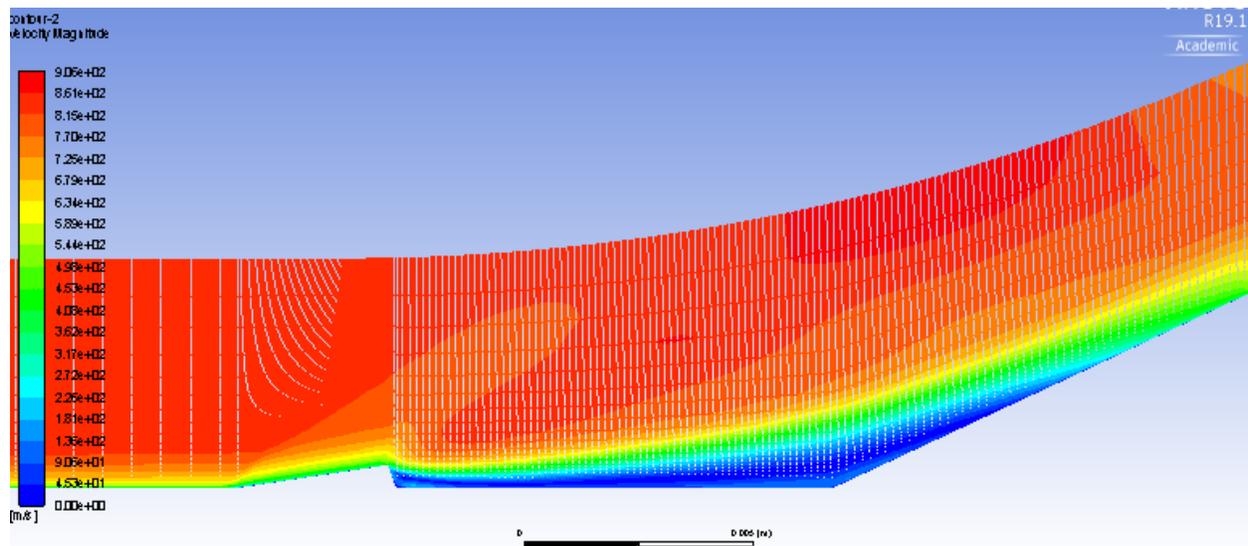

Figure 26 – Sample velocity contour plot of the RANS 0.5 case.
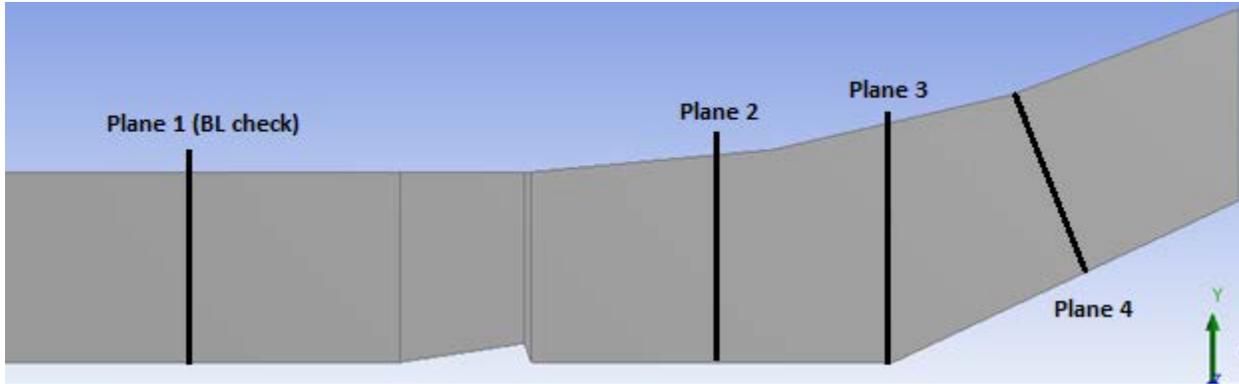
Figure 27 - View of the locations of the planes where velocity data was taken.
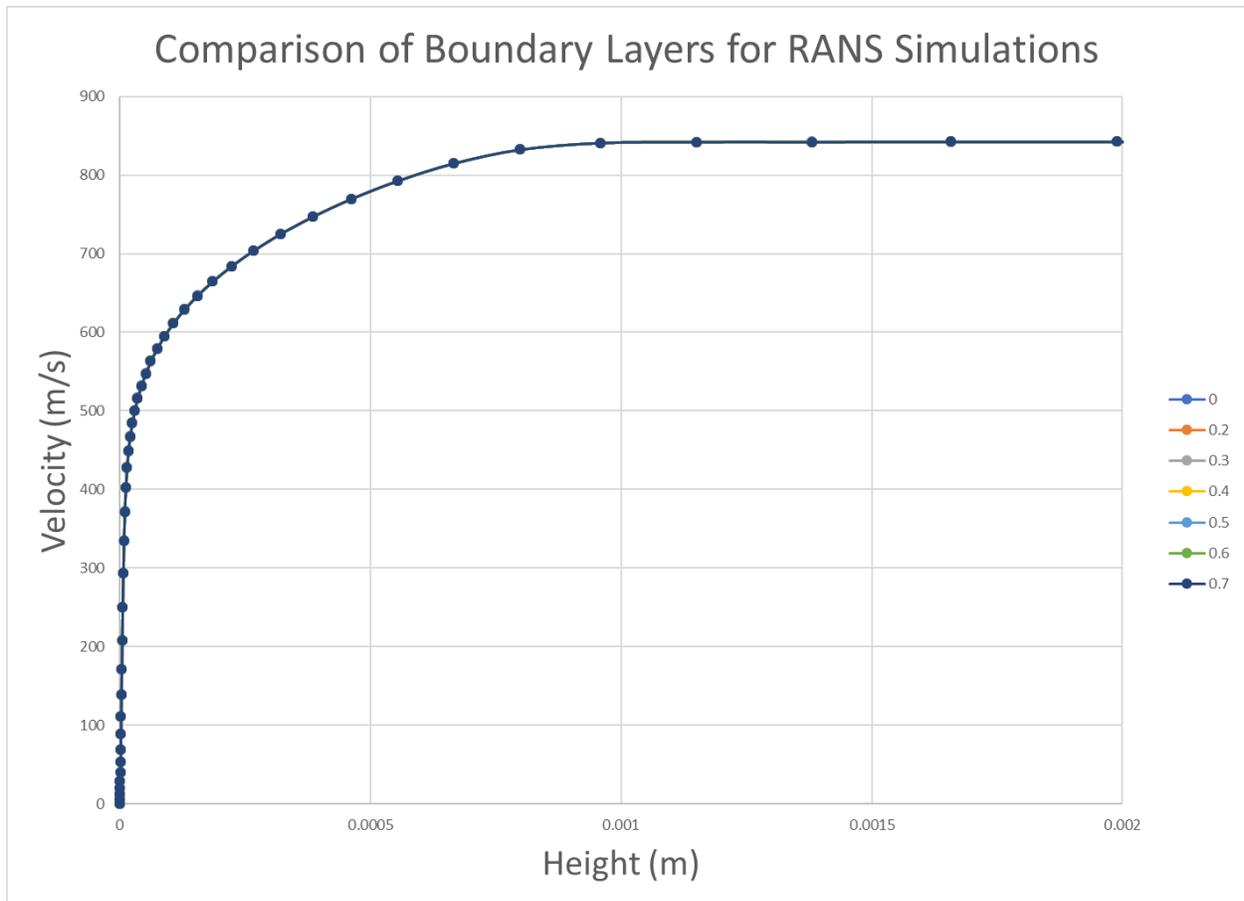
Figure 28 - Velocity profiles taken at Plane 1 for each RANS case.
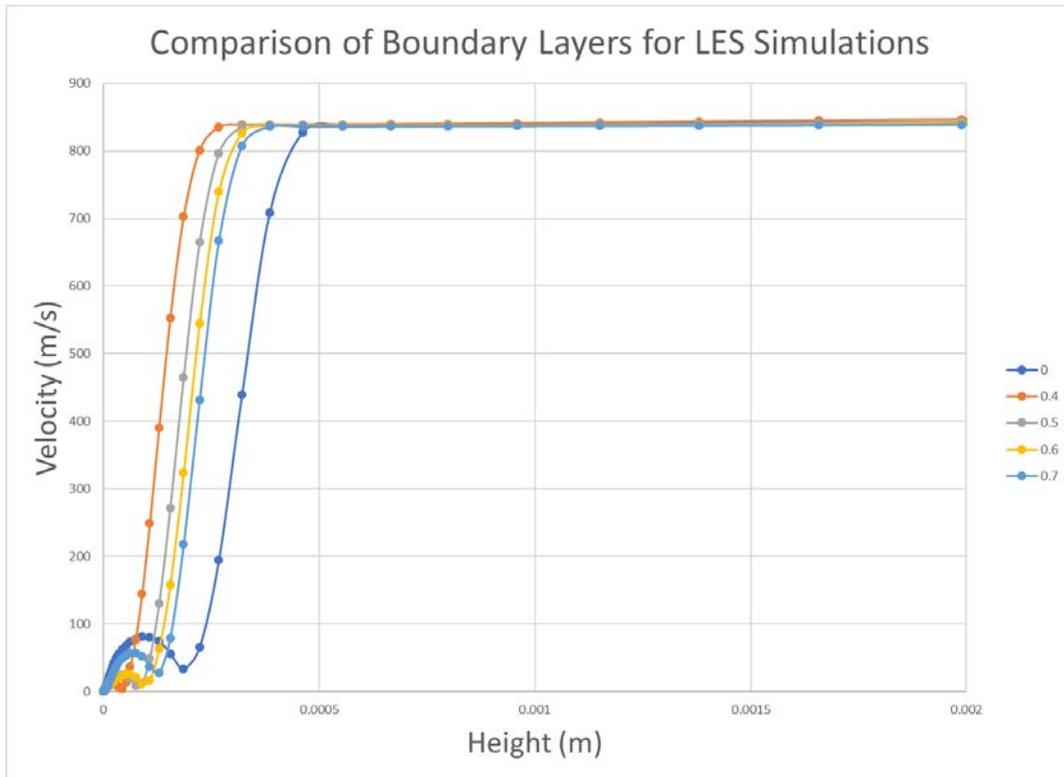
*Figure 29 - Velocity profiles taken at plane 1 for each LES case.*
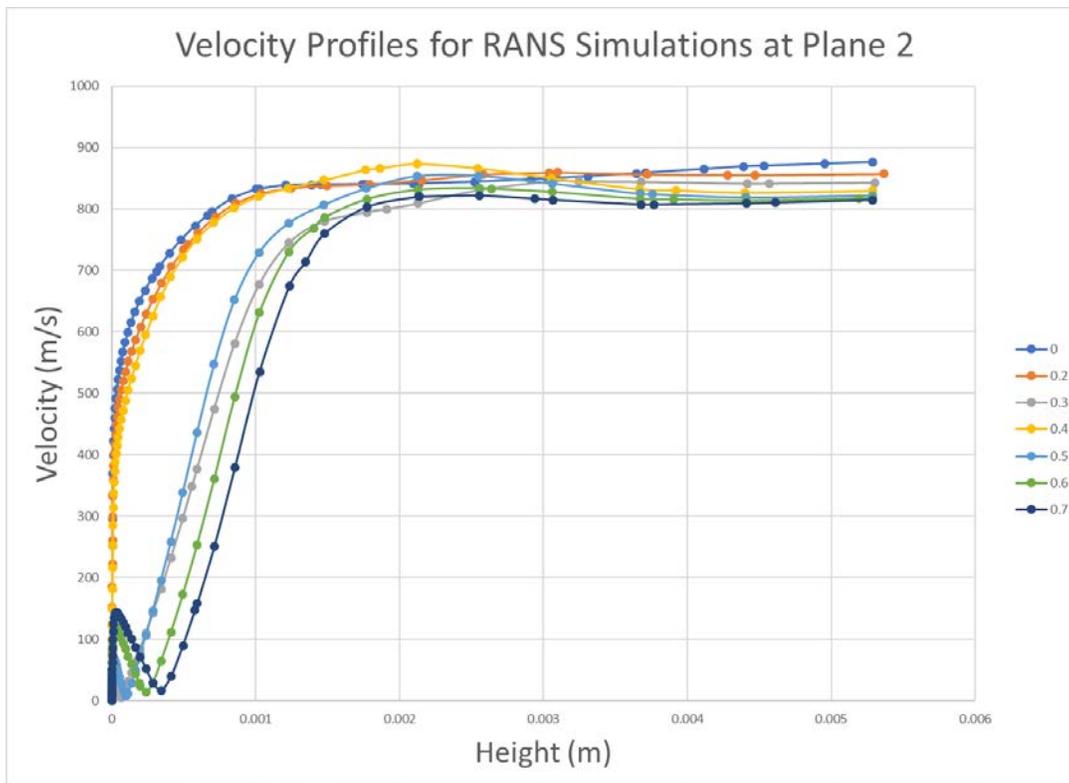
*Figure 60 - Velocity profiles for RANS simulations at plane 2.*
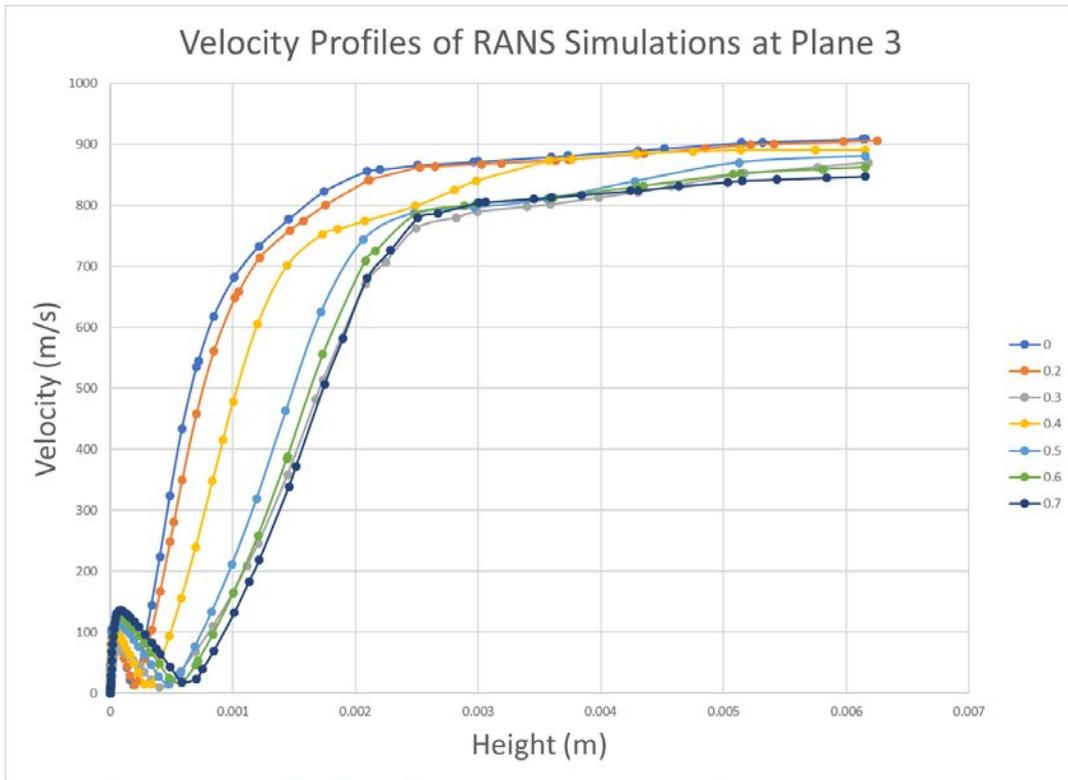
*Figure 31 - Velocity profiles for RANS simulations at plane 3.*
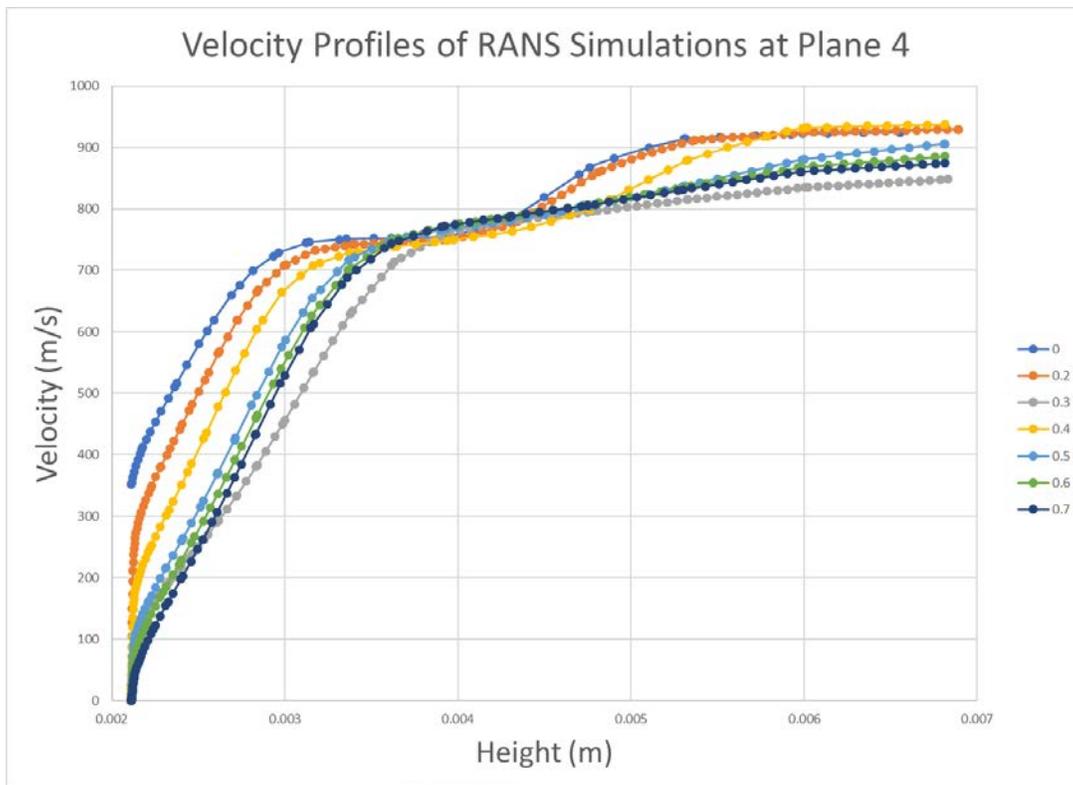
*Figure 32 - Velocity profiles for RANS simulations at plane 4.*
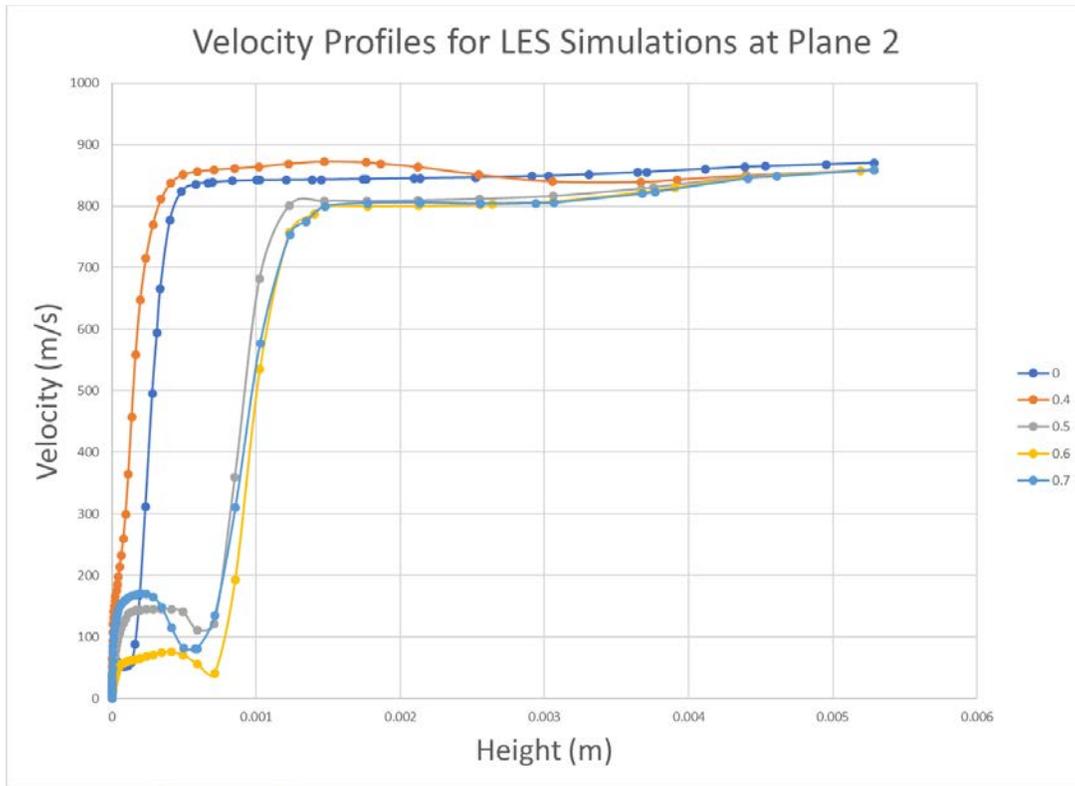
*Figure 33 - Velocity profiles for LES simulations at plane 2.*
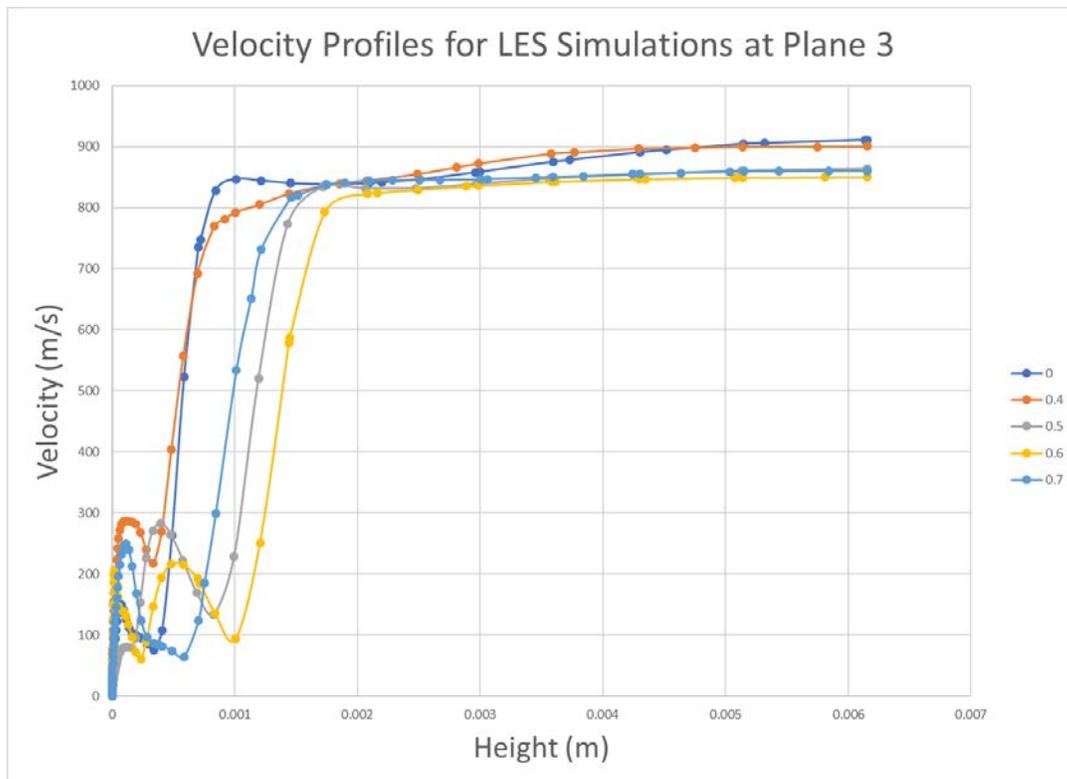
*Figure 34 - Velocity profiles for LES simulations at plane 3.*
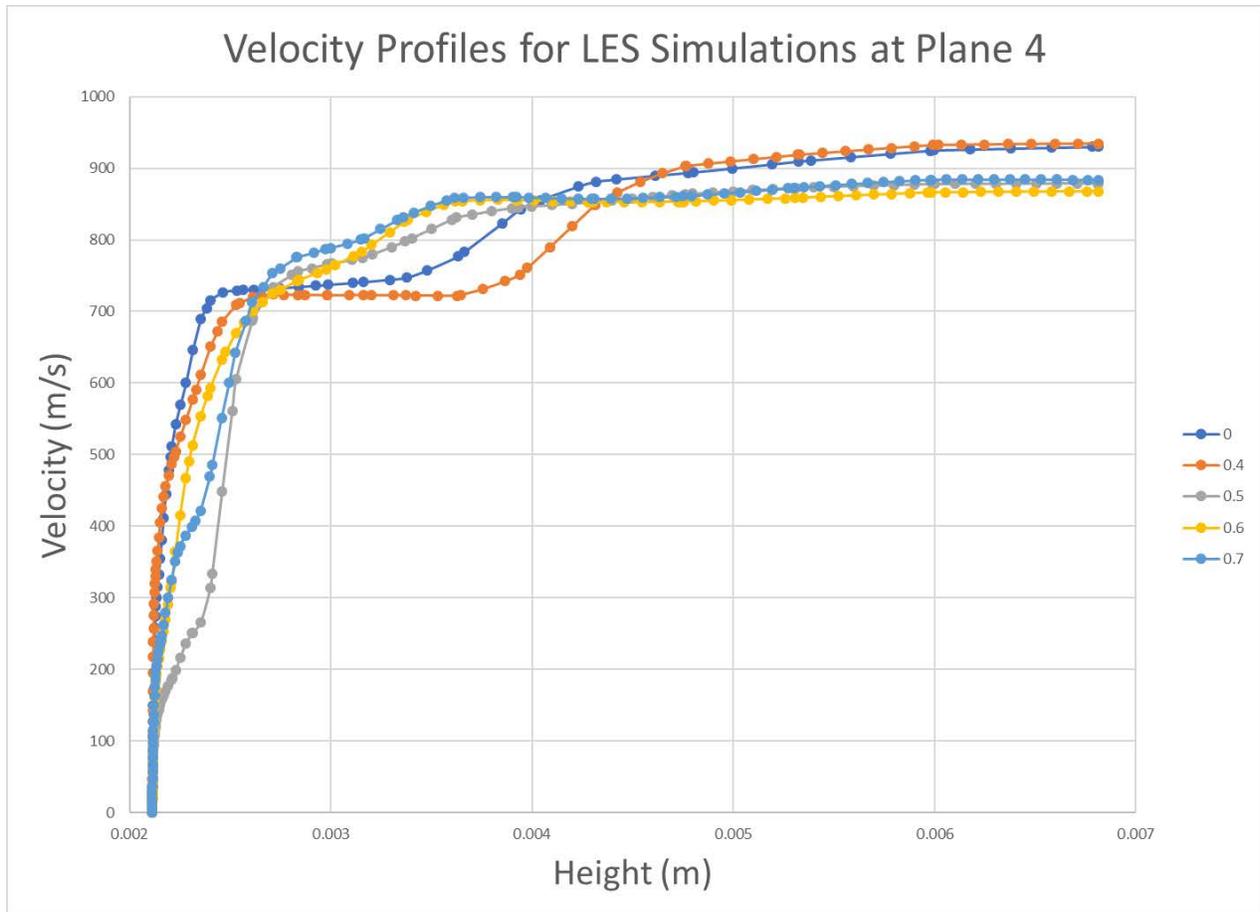
Figure 35 - Velocity profiles for LES simulations at plane 4.

4.2 3D RESULTS

The following results are a few screenshots from the 3D simulations. Figure 36 shows the pressure contour results from a primary simulation run with just the ramp and no MVG. The latter figures show the intermediate velocity contours of the $h/\delta = 0.5$ case. No velocity data was taken as for the 2D simulations for reasons that will be discussed in the next section.
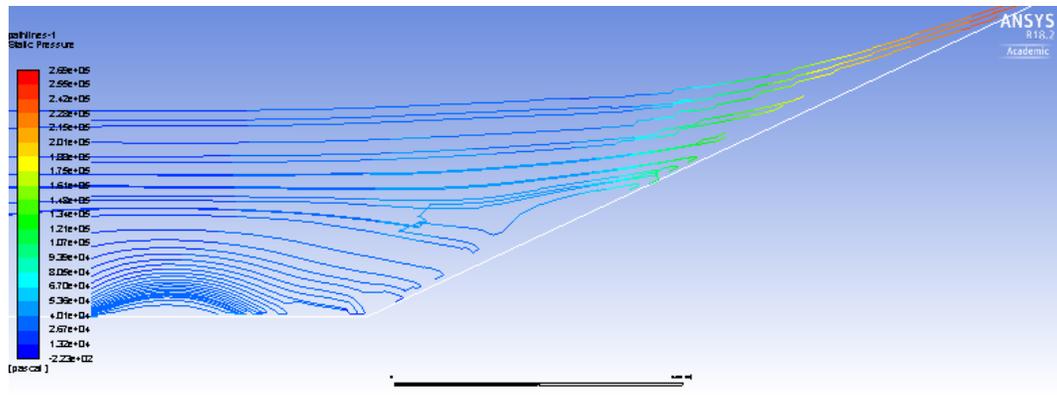
*Figure 36 - Pressure contour for the mid plane of the 3D ramp-only case.*
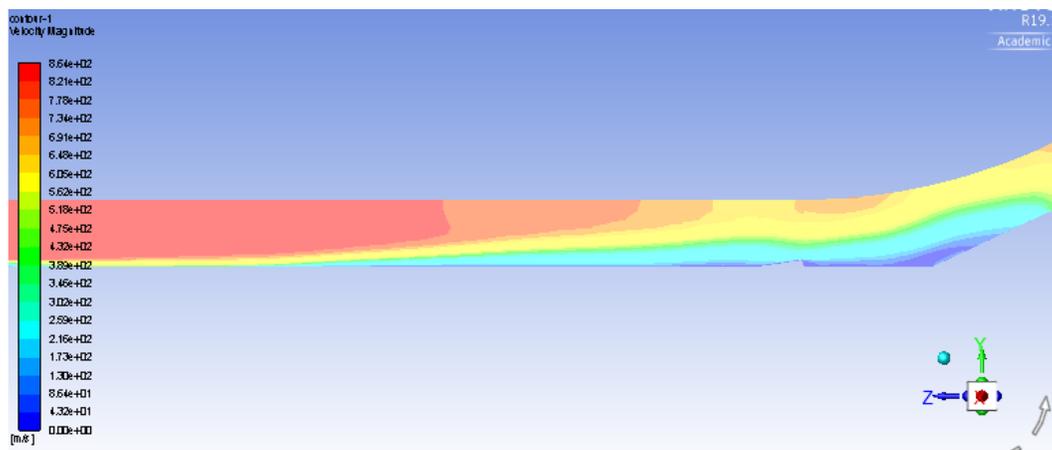
Figure 37 - Mid section view of the 3D simulation showing the velocity contours.
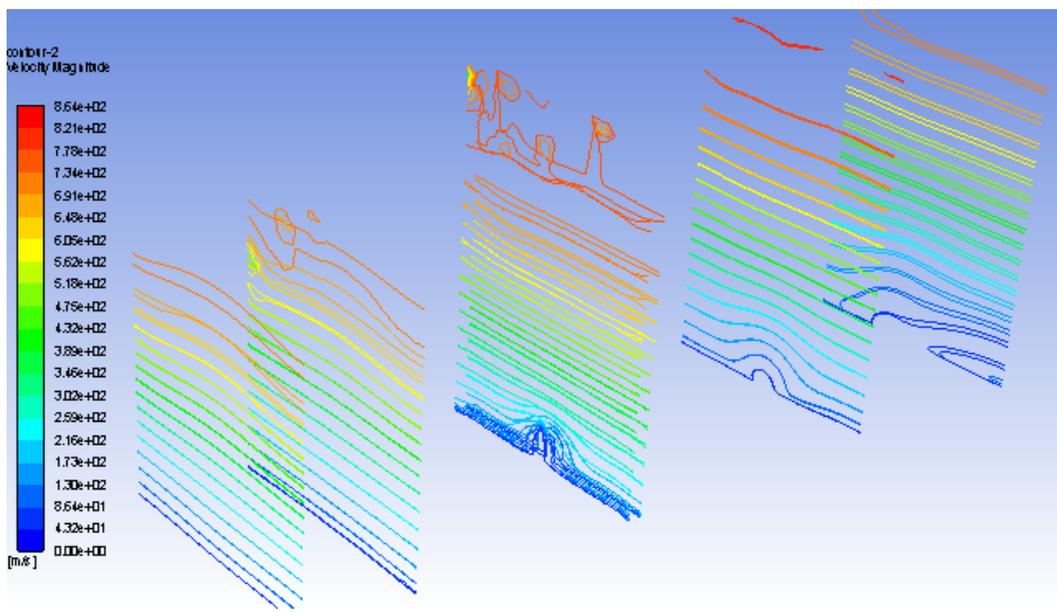

Figure 38 - Velocity section views normal to the flow at the interfaces between regions.

DISCUSSION

5.1 2D SIMULATIONS

5.1.1 Boundary Layer Confirmation

Figure 28 shows the boundary layer at the original inlet for the various RANS

simulations. Only the results for one simulation can be seen, yet all are plotted. This means that

the values are the same for each case and, therefore, the heights of the MVGs are what are

expected; e.g., an MVG with an h/δ value of 0.5 really is half the height of the incoming

boundary layer.

The boundary layers for the LES cases do not match as well as the RANS cases. The

variances are most likely due to the simulations' convergence. As the convergence was based on

oscillations and not a certain value, the simulations were stopped at different times, rendering

slightly different values. There is also an odd trend where the velocity profile increasingly

matches the no-MVG case with increasing MVG height. This is opposite of what is expected, as

a larger MVG should disrupt the flow more. Regardless of the reason, the profiles are different

for each case, meaning that the actual MVG height is slightly different than the expected height.

This casts doubt on the LES solutions as the supposed MVG height is slightly different than what

they should be.

Another noteworthy feature of the LES BL confirmation plot occurs near the wall. There

is a small "bump" in the profile that becomes larger with increasing MVG height. These plots are

of velocity magnitude and not simply velocity, meaning that these "bump" values could be

positive or negative. Having backflow in the boundary layer does not entirely make sense, but

perhaps is somewhat feasible due to the unsteady nature of the solver simulation.

5.1.2 Pressure and Velocity Contours

The MVGs in every RANS case exhibit the expected behavior. A shock wave forms over the MVG followed by an expansion fan where the MVG ends. Similar behavior is shown in Figure 4, although there are no trailing vortices in the simulations. There are also no obvious shock waves at the ramp except for the 0.2 and 0.4 cases. It is possible that the 0.3 case would have a shock wave but this case seems to be an anomaly within the RANS scenarios.

It should also be noted that the shock wave tends to curve toward the inlet. This is simply due to the geometry. In an attempt to avoid a prominent expansion fan, the top wall is curved. This increases the cross-sectional area which increases the flow velocity for supersonic flows. This is why the highest velocity is seen close to the outlet ahead of the shock wave and not at the inlet.

It is interesting to note that while the higher valued RANS cases did not show a prominent shock wave at the ramp corner, the LES simulations did. In fact, every LES simulation exhibits a shock wave at both the MVG and the ramp corner. It should not be forgotten, though, that these shocks at the ramp are formed in part due to the increase in velocity in that area and the shock near the ramp corner becomes less prominent with increased MVG height. As the LES simulations are time dependent, there is also, in general, higher vorticity and variability shown throughout the LES simulations.

5.1.3 RANS Simulations

The RANS velocity profiles at plane 2 follow a general trend. As the MVG height increases, the boundary layer height also grows, although not at the same rate. For the lower heights (h/δ = 0-0.4), this rate is incredibly small but still detectable. For the upper heights, the

growth is more dramatic with about a 0.0001-0.0002-meter difference. The upper heights also

show the "bump" close to the wall as demonstrated in the LES plane 1 simulations.

The plane 3 results follow the same trend as for plane 2 except now each case has a

"bump" and the boundary layer is larger. The BL difference between the extreme cases are also

not as great as they are for those of plane 2.

The plane 4 results are taken after the shock wave and demonstrate an interesting trend.

Every case starts with essentially the same value but an increase in MVG height causes the

velocity to increase faster for a given height. This is also the only plane where each case

intersects at a single point (at 0.00366 meters). This would make sense if there was a definite

shock wave present as in the LES cases but the RANS simulations do not have that trend.

Overall, the data for the RANS simulations is fairly consistent and logical. The "bump"

gets larger at the ramp corner as this is where the boundary layer and shock wave interact the

most. There is also a pattern where the greatest difference in results between any two heights

always occurs between the 0.4 and 0.5 cases. Perhaps there is some significance within this range

of heights.

The main anomaly out of these simulations is the 0.3 case which does not follow the

trends at any of the planes. There is a possibility that this height truly causes such a large shift in

the boundary layer but it is more probable that some error was committed in its analysis. These

results should be verified in future research.

5.1.4 LES Simulations

As the reader may have noticed, there are fewer simulations for the LES cases than for

the RANS cases. The simulations for the 0.2 and 0.3 cases were unable to converge. This came

as a surprise as it would seem that a smaller alteration in the geometry would be easier for the

solvers to handle than a large one. This was not the case. Fortunately, results for the other cases

came through and there is still sufficient evidence to draw some conclusions about the flow

behavior and compare it with the RANS simulations.

All the same trends noted for the RANS cases carry over for the LES cases. The main

difference is the variability of the cases. In the RANS simulations, a steady progression could be

seen from case to case; the BL height was greater for the 0.5 case than the 0.4 case, the 0.6 case

than the 0.5 case, etc. However, the LES cases showed no such pattern as the BL heights were

not in sequential order according to the MVG height. This is most likely due to the time

dependent nature of the solver and the difference in convergence time, as mentioned previously.

The other notable difference can be seen in plane 4. The curves still all intersect at a point

as in the RANS case but this point has moved to about 0.0026 meters. Looking at the pressure

and velocity contours, this is approximately where the shockwave occurs, explaining the

similarity in values.

5.2 3D SIMULATIONS

A primary 3D geometry consisting of just the ramp was created as somewhat of a

benchmark for the 3D simulations. The mesh for this geometry was able to be completely

structured as there were no nonrectangular parts to complicate the mesh production. This

simulation converged and produced results similar to those shown in Figure 39 below by Yan et

al. (2017).

Unfortunately, the 3D simulations with the MVG did not converge. Initial and

intermediate results were obtained but eventually and inevitably, the solver equations hit a point

of positive reinforcement and gave impossible outcomes. Changing the time step, solving

methods, and relaxation constraints delayed the divergence somewhat but still failed to give

reasonable results.
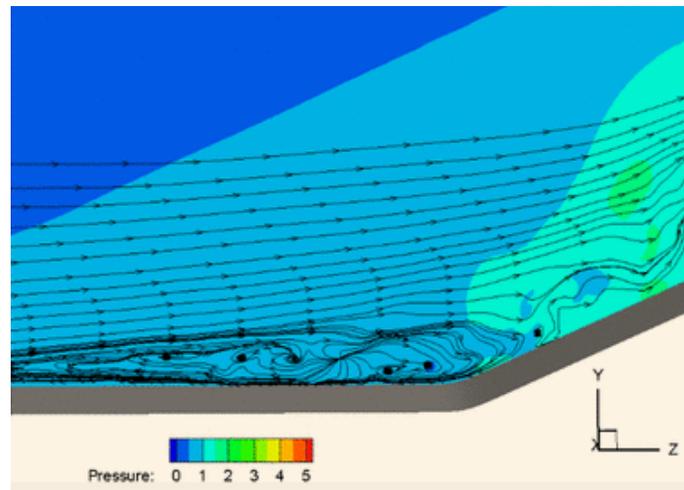
Figure 39 - Pressure contours of the mid plane for the ramp alone performed by Yan et al., (2017). Compare with Figure 36.

The main estimation for why this happened is the cell size of the mesh. Being limited in

cell count, the cells were most likely too large to successfully capture the complicated flow of

the vortices and the shock waves. Also, as a structured mesh could not be generated around the

MVG itself, a relatively large discontinuity existed upon entering and leaving that region. These

discontinuities make it difficult for the flow to become resolved and contribute to the divergence

of the residuals.

While the simulations did not converge, the results shown give slight evidence of

representing a true-to-life solution. The mid-section view is very similar to intermediate views of

the 2D solutions, with the initial velocity penetrating more of the flow field with time. The cross-

sectional plane views also show a "notch" in the flow after the MVG, giving evidence that the

MVG upstream has had an effect on the downstream velocity profile. The furthest plane of

Figure 38 shows an offset, asymmetrical flow as well. Either this section had yet to fully resolve

and feel the effects of the MVG or this asymmetry shows the initial forming of one of the

vortices.

CONCLUSIONS AND FURTHER RESEARCH

Several conclusions can be made with the presented data. The first is that the BL height increases with MVG height but not at the same rate. This growth rate also seemed to decrease slightly for the upper heights. The second is that the LES simulations gave more accurate results than the RANS ones as a shock wave was much more prominent.

Unfortunately, not much can be said for the 3D simulations other than the fact that the ramp-only case matched with previous data. Without this 3D data, an optimal MVG height cannot be determined. The 2D simulations give a good initial glance into the effects of MVGs; but as they are only 2D, no vortices form, making it difficult, if not impossible, to determine a definite optimal MVG height.

The lack of results also makes it difficult to compare to any benchmarks. There is plenty of data to compare 3D results with but only the 2D results were obtained. It would be possible to compare the 2D results with 2D benchmarks but as this was not the objective of the subject, no 2D benchmarks for this situation were found.

The data does gives way for more questions to ask and more simulations that could be run. The first and most obvious change that could be made would be to use a software that allows for a sufficiently high cell count. While the software worked well for the 2D simulations, it did not provide enough elements to allow the 3D simulation solve. The primary 3D ramp case could be solved but that was because the flow was rather uniform up until the ramp, meaning that a much lower cell count could be used for a majority of the geometry.

The act of adding the extra length to the original geometry also exacerbated the limited cell issue. It is possible to import a velocity profile for 2D simulations but it was unknown how to apply a profile for 3D simulations. There was also no guarantee that the profile would be

turbulent instead of laminar. This is what necessitated the extra length. Regardless, a different, or

at least, professional, version of the software would be needed to accurately model the flow.

Barring the cell limit, there are plenty of improvements that could be made with the 2D

cases. One of these factors was the location of the ramp with respect to the MVG. The geometry

was modeled such that the angles of the MVG were consistent for each case. In exchange, this

altered the length between the end of the MVG and the ramp corner. If it is desired to have

results which are perfectly comparable, this length difference should be accounted for. Instead of

a fixed length from the front of the MVG, it should have a consistent length measured from the

back of the MVG as this distance effects the strength of the vortices and boundary layer.

Looking at the collected data, the next obvious action to take would be to redo the

anomalies. The 0.3 cases for the RANS simulations are seemingly out of place at each plane. It is

recommended to either re-run this case or perhaps give the solution more time to converge. If

time permitted, it would also be beneficial to re-run other cases from the beginning to verify the

current results.

In addition to re-running some cases, it is recommended to give the LES simulations

more time to converge. The simulations were run on a single computer with moderate processing

power. This allowed for the calculation of only a few iterations a second for the 2D cases and

about one iteration every few seconds for the 3D case. It would be valuable to run a few LES

simulations on a supercomputer or a computer with more processing power to see if the residuals

converged any better after many more iterations.

One of the trends mentioned in the previous section was the jump in values between the

0.4 and 0.5 cases. Further simulations could be run for values between these two to see if there is

a linear progression as exhibited by the other cases. These values are also some of the more

popular choices for past research, possibly implying that some unique phenomena occur around these values of MVG height.

Finally, there are two aspects of the plane 4 data that could be enhanced. First, from the data, it appears that the entirety of the BL was not recorded as the velocity information starts at 0.002m. Obviously there is some data between that height and the wall as seen from the other plane data. It is not expected that this data would show anything surprising but it cannot be discounted without examining it. Secondly, the intersection point of the plane 4 data for the RANS simulations could be more closely studied. Perhaps a shock wave or some other flow property does exist that is not immediately apparent. Further simulations could look into the reason why this intersection point happens.

REFERENCES

Anderson, J. D., Jr. (2001). *Fundamentals of Aerodynamics* (3rd ed.), New York, NY.

Babinsky, H., Li, Y., & Pitt Ford, C.W. (2009). Micro-ramp control of supersonic oblique shock wave/boundary-layer interactions. *AIAA Journal*, 47(3), 668-675.

Cengel & Cimbala (n.d.). The Turbulent Flat Plate Boundary Layer. Retrieved November 26, 2018, fromhttps://www.mne.psu.edu/cimbala/me320web_Spring_2015/pdf/Flat_plate _turbulent_BL.pdf

Holden, H. & Babinsky, H. (2007). Effect of microvortex generators on separated normal shock/boundary layer interactions. *J. Aircraft*, 44(1), 170–173.

Li, Q. & Liu, C. (2011). Implicit LES for supersonic micro-ramp vortex generator: new discoveries and new mechanisms. *Modell. Simul. Eng*., 934982.

Lu, F.K., Pierce, A.J., & Shih, Y. (2010). Experimental study of near wake of micro vortex generators in supersonic flow. *AIAA Journal*, 4623.

Martis, R.R. & Misra, A. (2013). Effect of height of microvortex generators on swept shock wave boundary layer interactions. *CEAS Aeronautical Journal*, 4(3), 315-326.

Meunier, M. & Brunet, V. (2008). High-lift devices performance enhancement using mechanical and air-jet vortex generators. *J. Aircraft*, 45(6), 2049-2061.

Panaras, A. G. & Lu, F. K. (2015). Micro-vortex generators for shock wave/boundary layer interactions. *Progress in Aerospace Sciences*, 74, 16-47.

Pearcey, H.H. (1961). Shock-induced separation and its prevention by design and boundary layer control. *Boundary Layer and Flow Control*, 2.

Reynolds Averaged Approach vs. LES. (2009, September 20). Retrieved November 26, 2018, from http://www.afs.enea.it/project/neptunius/docs/fluent/html/th/node45.htm

Titchener & Babinsky (2013). Shock wave/boundary layer interaction control using a

      combination of vortex generators and bleed. *AIAA Journal*, 51(5), 1221–1233.

Titchener, N. & Babinsky, H. (2015). A review of the use of vortex generators for mitigating

      shock-induced separation. *Shock Waves*, 25(473).

Troia, T.J., Patel, A.A., Crouse, D., & Hall, G.R. (2011). Passive device flow control for normal

      shock/boundary layer interactions in external compression inlets. *AIAA Journal*, 3911.

Wang, B., Liu, W.D., Zhao, Y.X., Fan, X.Q., & Wang, C. (2012). Experimental investigation of

      the micro-ramp-based shock wave and turbulent boundary layer interaction control. *Phys.*

      Fluids, 24.

Yan, Y., Chen, L., & Li, Q. (2017). Numerical study of micro-ramp vortex generator for

      supersonic ramp flow control at mach 2.5. *Shock Waves*, 27, 79.

LIST OF APPENDICES

APPENDIX A – Summary of previously performed research

APPENDIX B – Pressure and velocity contour results

APPENDIX A - Summary table of previous relevant research by Babinsky and Titchener.

Studies utilizing VGs for shock separation control

Reference	Year	Type of investigation	Wind tunnel	SBLI	M_∞	Re (m^{-1})
Lina and Reed [11]	1950	Flight test	–	Terminal shock on wing	$\simeq$ 1.0– 1.4	7.8 $\times$ 10^6
Griggs [22]	1958	Inlet study; canonical 2-shock axi. inlet	RAE no. 4 supersonic wind tunnels	Terminal and downstream (ds.) diffuser	2–3	12 $\times$ 10^6
Pearcey [20]	1961	Fundamental (Fund.) SBLI study	NPL supersonic facility	Terminal shock on two-dimensional bump	1–1.4	–
Edwards [23]	1966	Free-flight test	–	Terminal shock on airfoil	1.35	31 $\times$ 10^6
Gartling [26]	1970	Fund. SBLI study	University of Texas, Austin, Mach 5 facility	Compression corner (35°)	4.67	47 $\times$ 10^6
Mitchell [25]	1971	Inlet study; NASA 60/40 inlet	NASA John H. Glenn 10 ft. $\times$ 10 ft.	Oblique reflection, terminal and ds diffuser	2.5	6.2 $\times$ 10^6
McCormick [27]	1993	Fund. SBLI study	UTRC supersonic facility	Normal with ds. divergence	1.56– 1.65	15 $\times$ 10^6
Barter and Dolling [31]	1995	Fund. SBLI study	University of Texas, Austin, Mach 5 facility	Compression corner (28°)	5	52 $\times$ 10^6
Wasserbauer et al. [32]	1996	Inlet study; two-dimensional bifurcated mixed compression	NASA John H. Glenn 10 ft. $\times$ 10 ft.	Terminal and ds. diffuser	2.0– 2.8	7.2 $\times$ 10^6
Ashill et al. [35]	2001	Airfoil study	DERA 8 ft. high-speed facility	Terminal shock on airfoil	0.67– 0.71	30 $\times$ 10^6
Holden and Babinsky [37]	2007	Fund. SBLI study	CUED SST	Normal straight-channel	1.5	28 $\times$ 10^6
Babinsky et al. [47]	2009	Fund. SBLI study	CUED SST	Oblique reflection (7°)	2.5	40 $\times$ 10^6
Blinde et al. [51]	2009	Fund. SBLI study	Delft University TST-27 trans-supersonic facility	Oblique reflection (10°)	1.84	37 $\times$ 10^6
Bur et al. [38]	2009	Fund. SBLI study	ONERA Meudon Center S8Ch	Terminal shock on two-dimensional bump	1.45	14 $\times$ 10^6

Zare Shahneh and Motallebi [39]	2009	Fund. SBLI study	Queen Mary high-speed facility	Normal with ds. divergence	1.4	16×10^6
Herges et al. [52]	2010	Fund. SBLI study	University of Illinois supersonic wind tunnel	Normal with ds. divergence	1.4	30×10^6
Lee et al. [50]	2010	Fund. SBLI study	TGF Wright-Patterson Air Force Base	Oblique reflection (8°)	2.98	1.8×10^6
Titchener and Babinsky [42]	2011	Fund. SBLI study	CUED SST	Terminal shock and ds. diffuser	1.4	31×10^6
Rybalko et al. [43]	2012	Fund. SBLI study	CUED SST	Normal shock followed by ds. diffuser	1.4	26×10^6
Verma et al. [46]	2012	Fund. SBLI study	NAL trisonic blow-down facility	Compression corner (24°)	2	25.3×10^6
Herges et al. [53]	2012	Inlet study; Gulfstream inlet	NASA John H. Glenn 8 ft. × 6 ft.	Terminal with ds. diffuser	1.7–1.8	15.7×10^6
Titchener and Babinsky [44]	2013	Fund. SBLI study	CUED SST	Terminal shock and ds. diffuser	1.4	31×10^6

APPENDIX B – Pressure and velocity contour results

This appendix shows the pressure and velocity contour plots of the 2D simulations. The pressure plot is shown first followed by the velocity magnitude plot.

RANS CASES

h/δ = 0
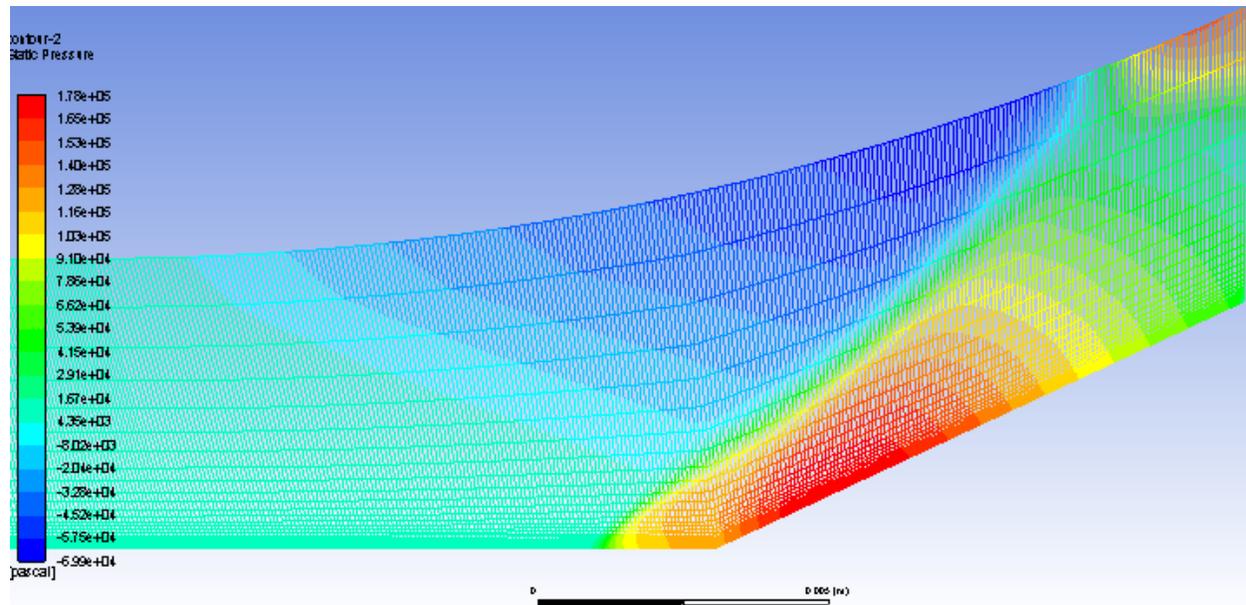
*Figure B1 – The 2D, RANS pressure contour plot results for the h/δ = 0 case.*
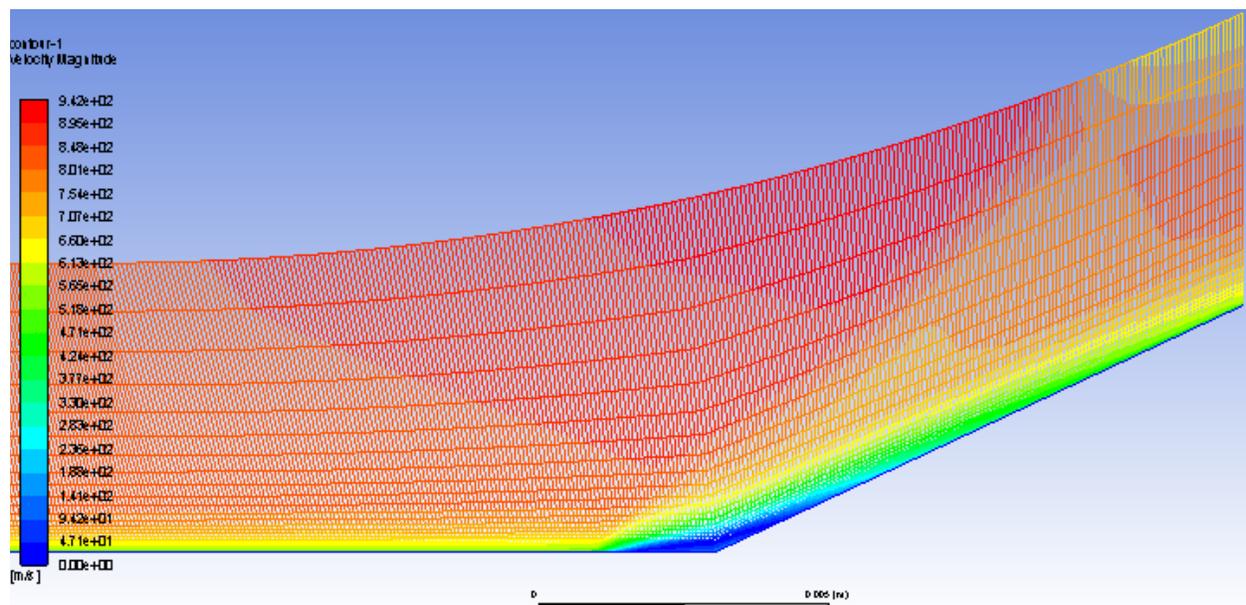
*Figure B2 – The 2D, RANS velocity contour plot results for the h/δ = 0 case.*

$h/\delta = 0.2$
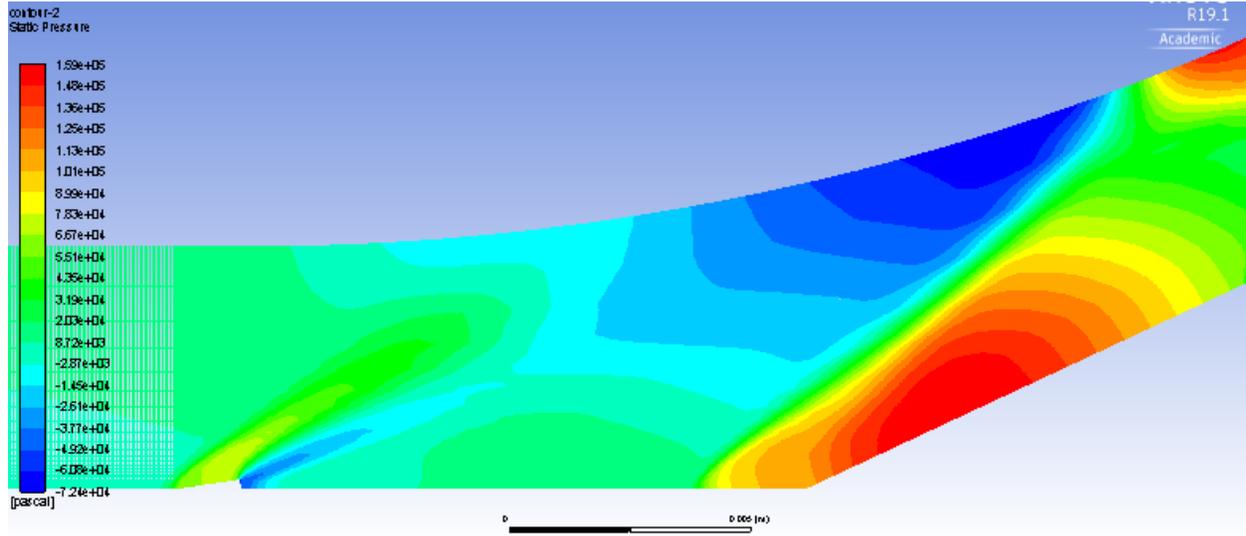
Figure B3 – The 2D, RANS pressure contour plot results for the h/δ = 0.2 case.
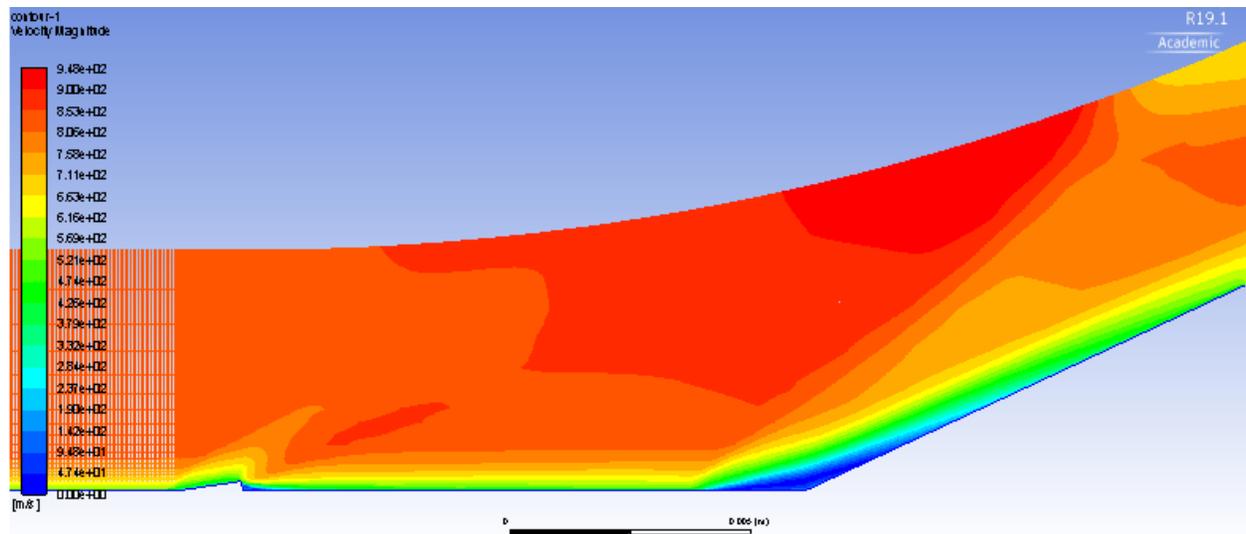
Figure B4 – The 2D, RANS velocity contour plot results for the h/δ = 0.2 case.

h/δ = 0.3
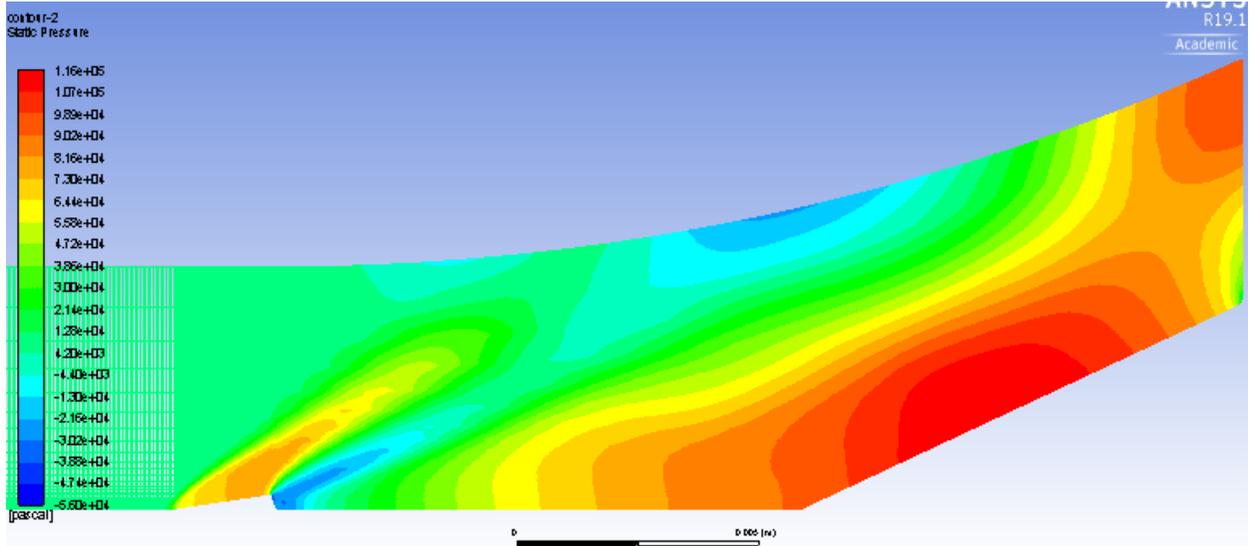
Figure B5 – The 2D, RANS pressure contour plot results for the h/δ = 0.3 case.
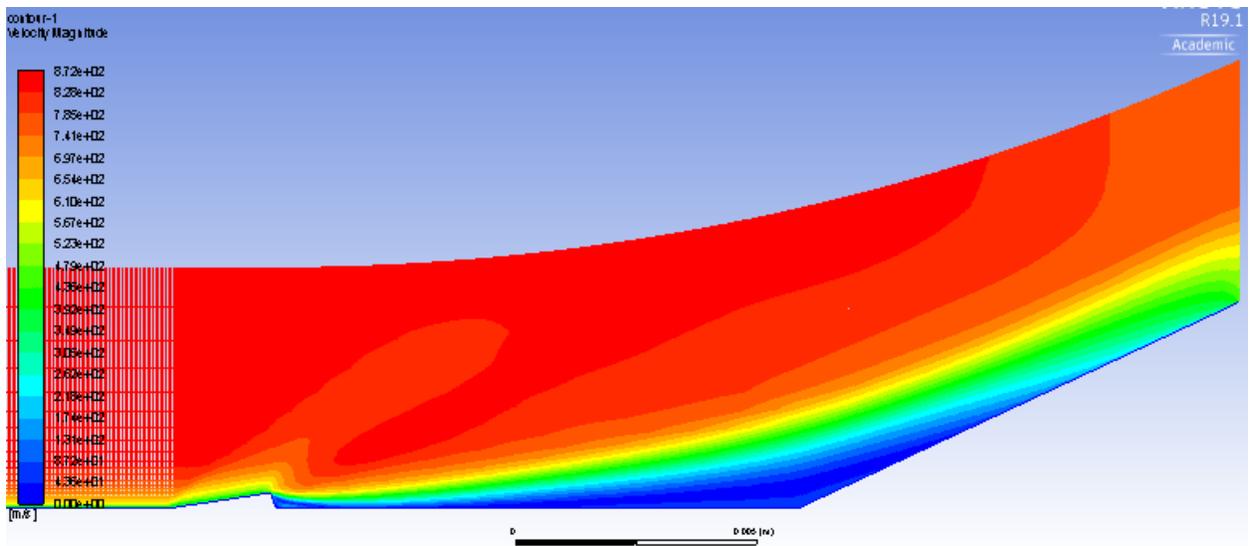
*Figure B6 – The 2D, RANS velocity contour plot results for the h/δ = 0.3 case.*

h/δ = 0.4
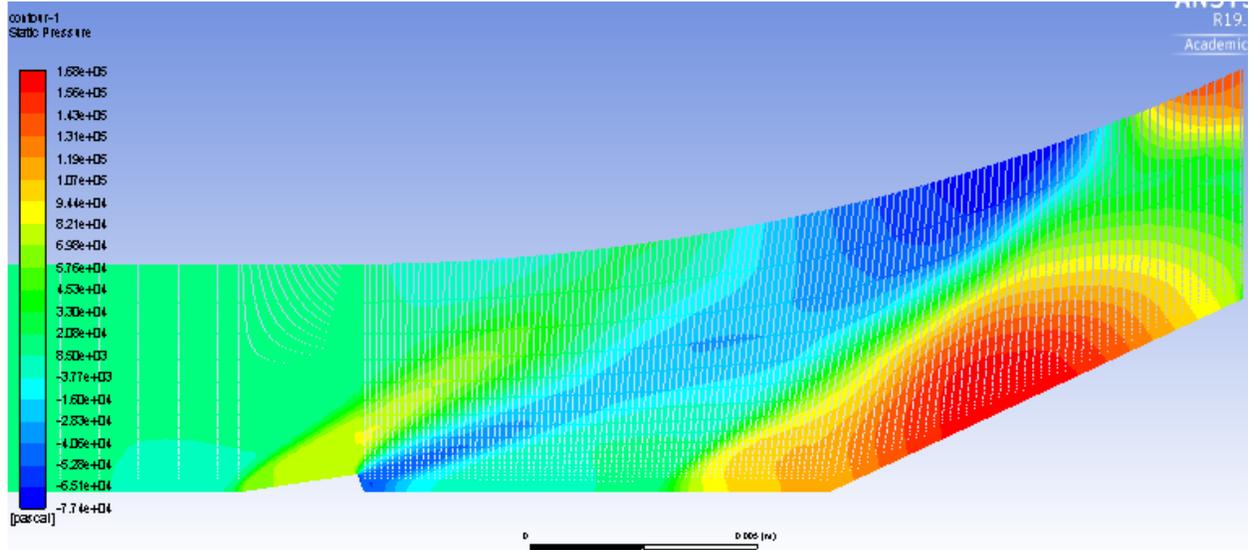
*Figure B7 – The 2D, RANS pressure contour plot results for the h/δ = 0.4 case.*
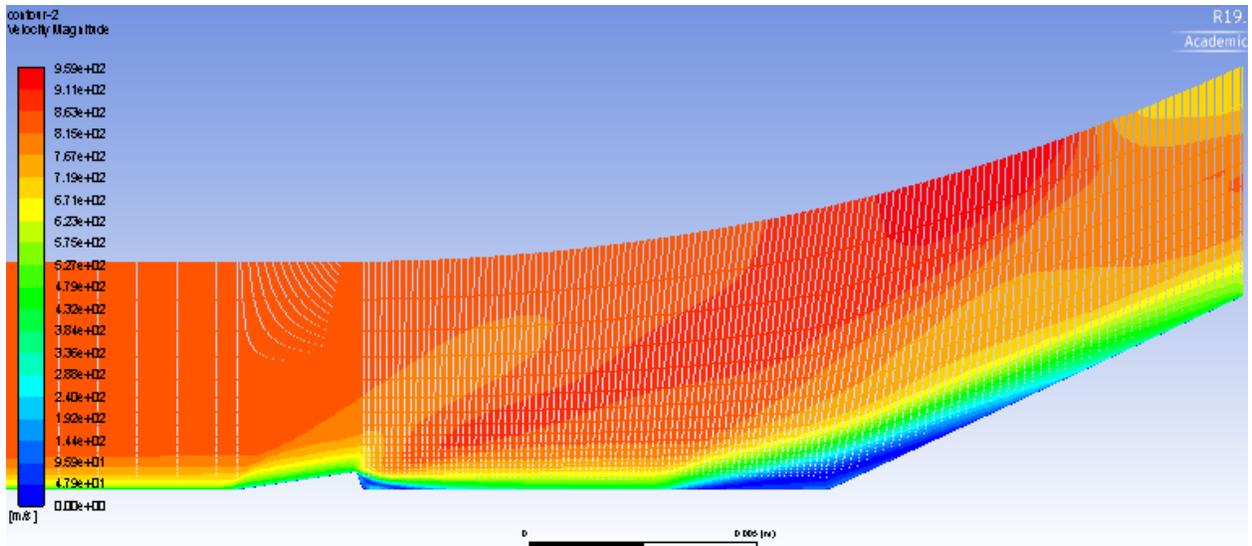
Figure B8 – The 2D, RANS velocity contour plot results for the h/δ = 0.4 case.

h/δ = 0.5
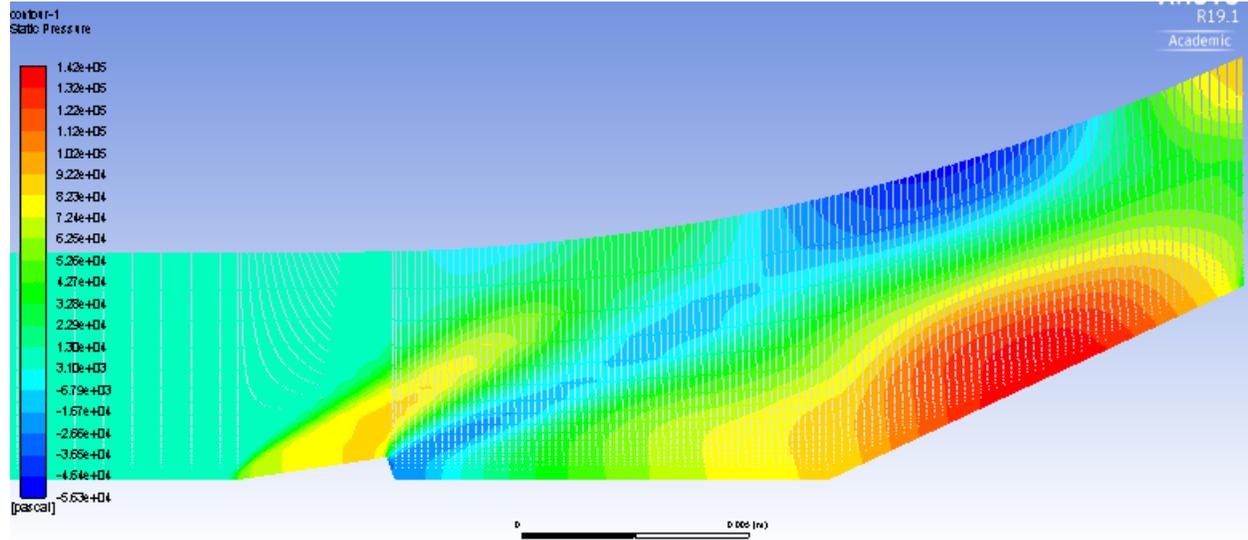
Figure B9 – The 2D, RANS pressure contour plot results for the h/δ = 0.5 case.
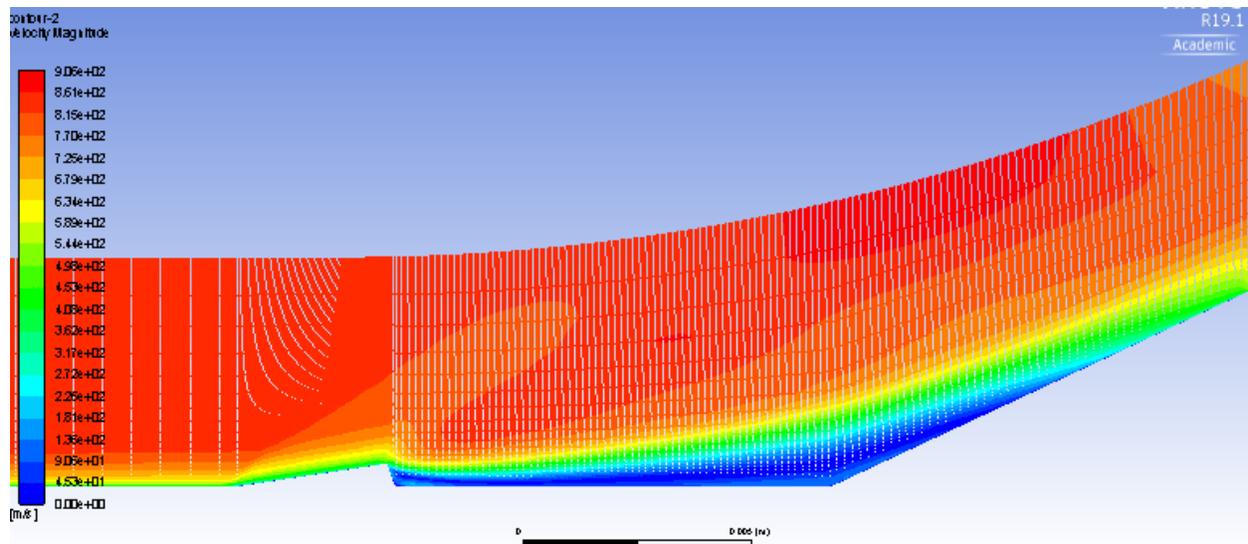
Figure B10 – The 2D, RANS velocity contour plot results for the h/δ = 0.5 case.

h/δ = 0.6
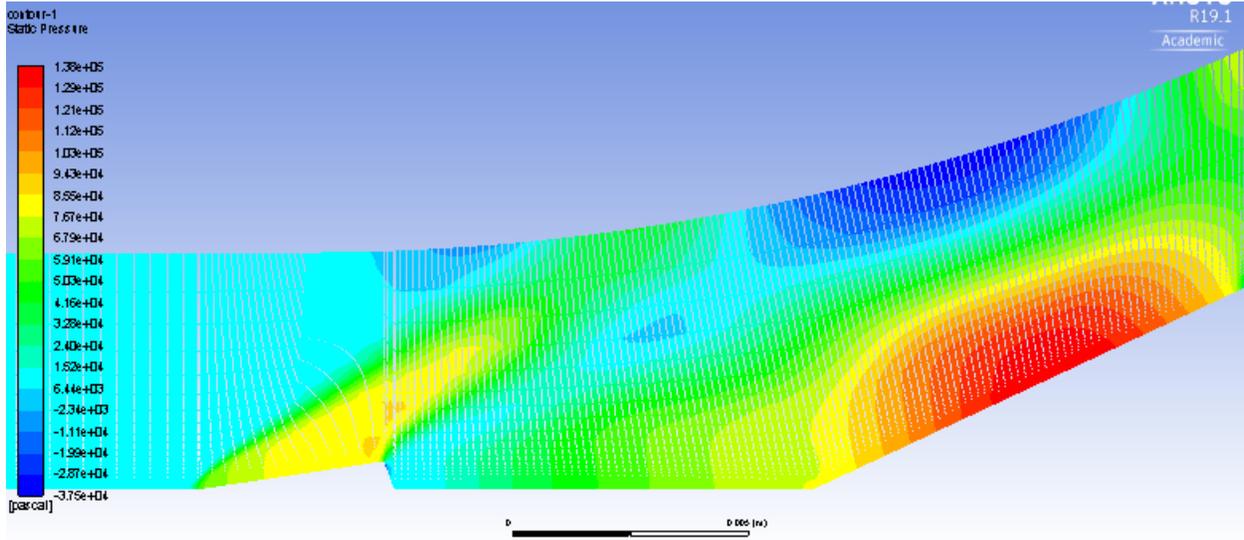
*Figure B11 – The 2D, RANS pressure contour plot results for the h/δ = 0.6 case.*
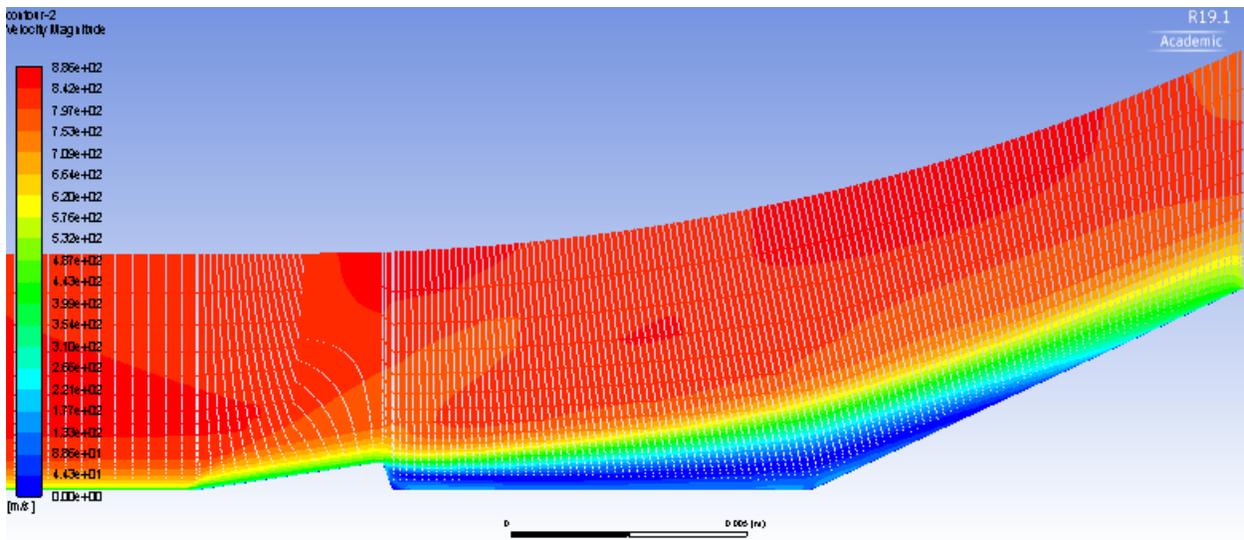
*Figure B12 – The 2D, RANS velocity contour plot results for the h/δ = 0.6 case.*

h/δ = 0.7
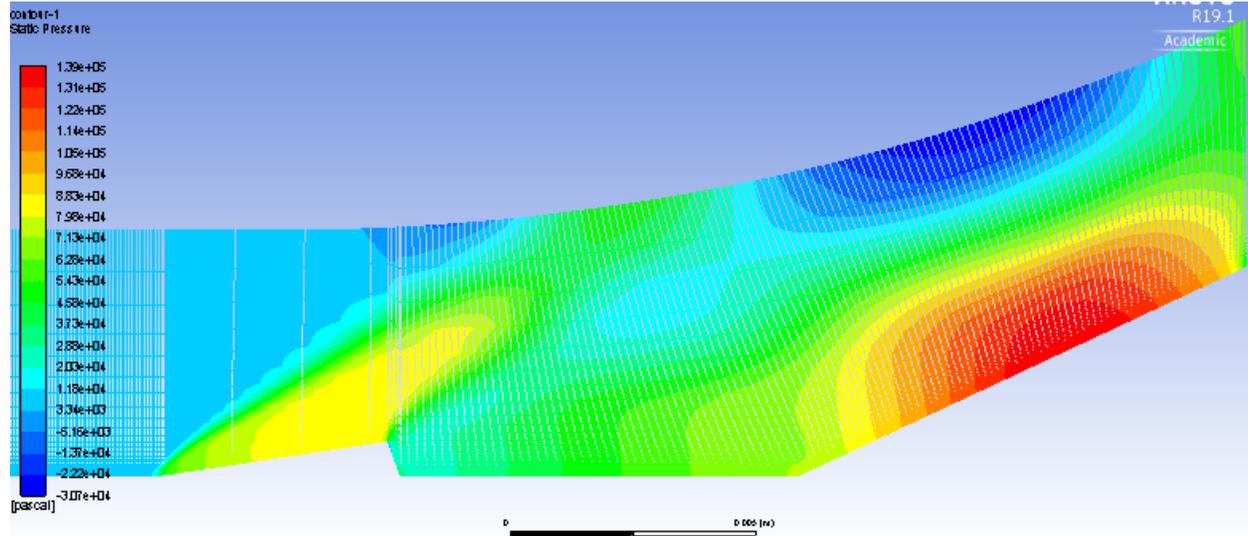
Figure B13 – The 2D, RANS pressure contour plot results for the h/δ = 0.7 case.
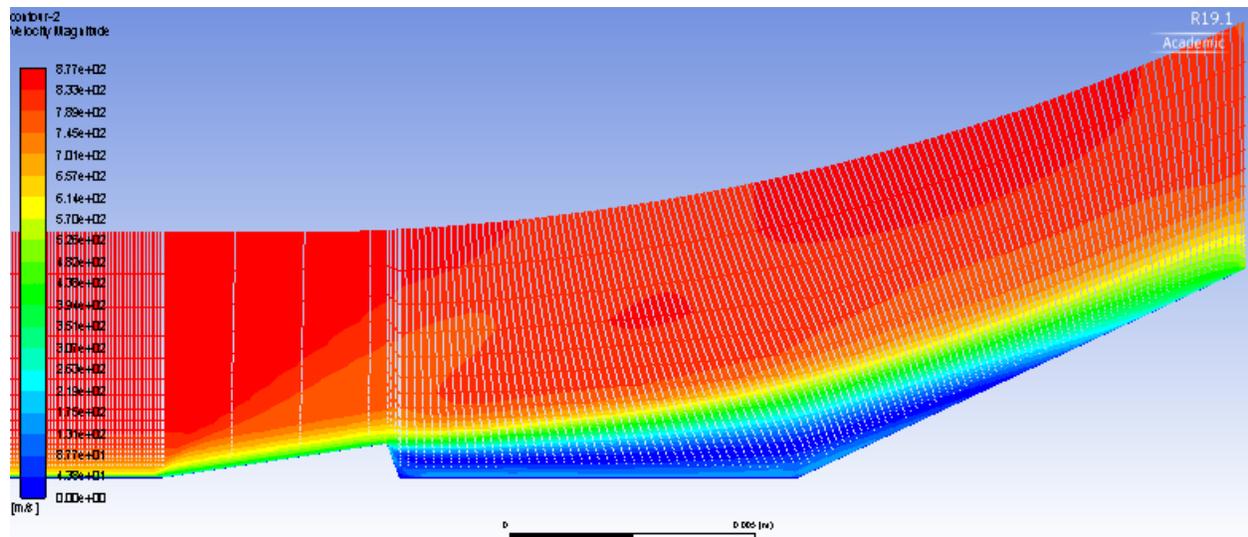
Figure B14 – The 2D, RANS velocity contour plot results for the h/δ = 0.7 case.

LES CASES

h/δ = 0
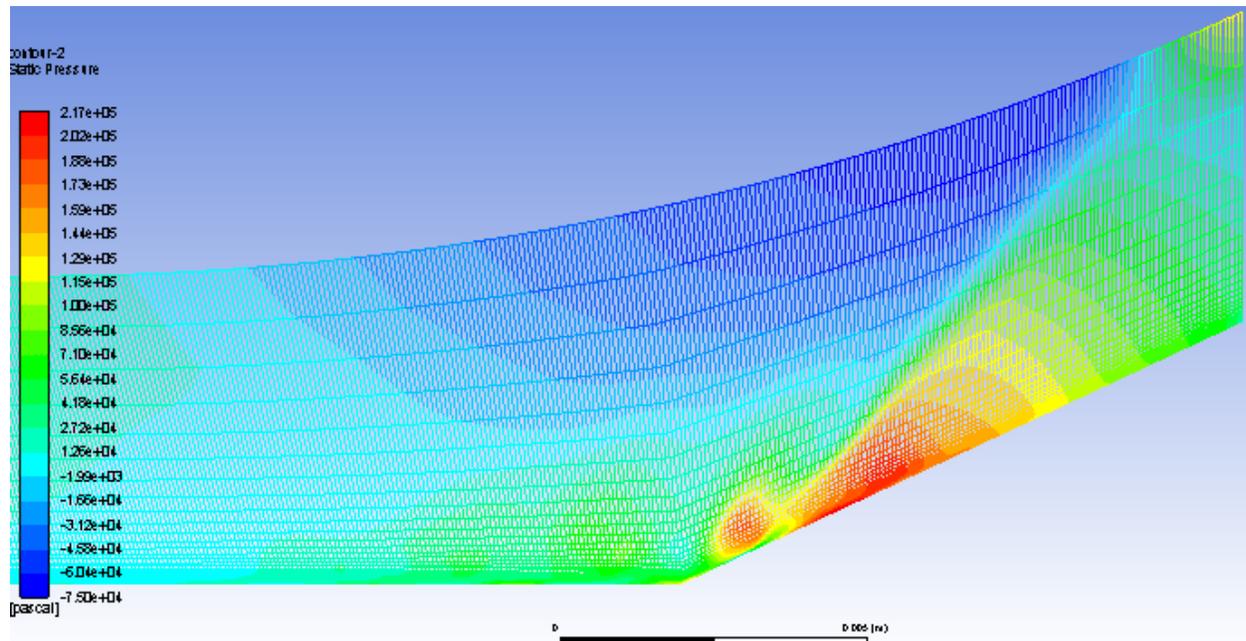
Figure B15 – The 2D, LES pressure contour plot results for the h/δ = 0 case.
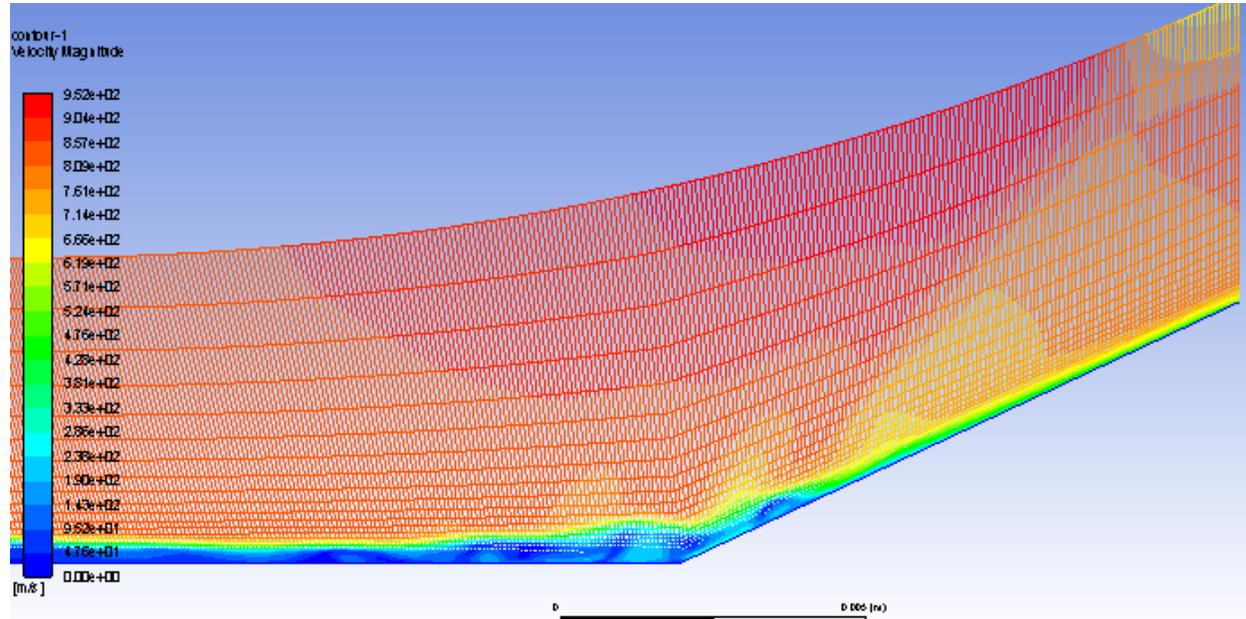
Figure B16 – The 2D, LES velocity contour plot results for the h/δ = 0 case.

h/δ = 0.4
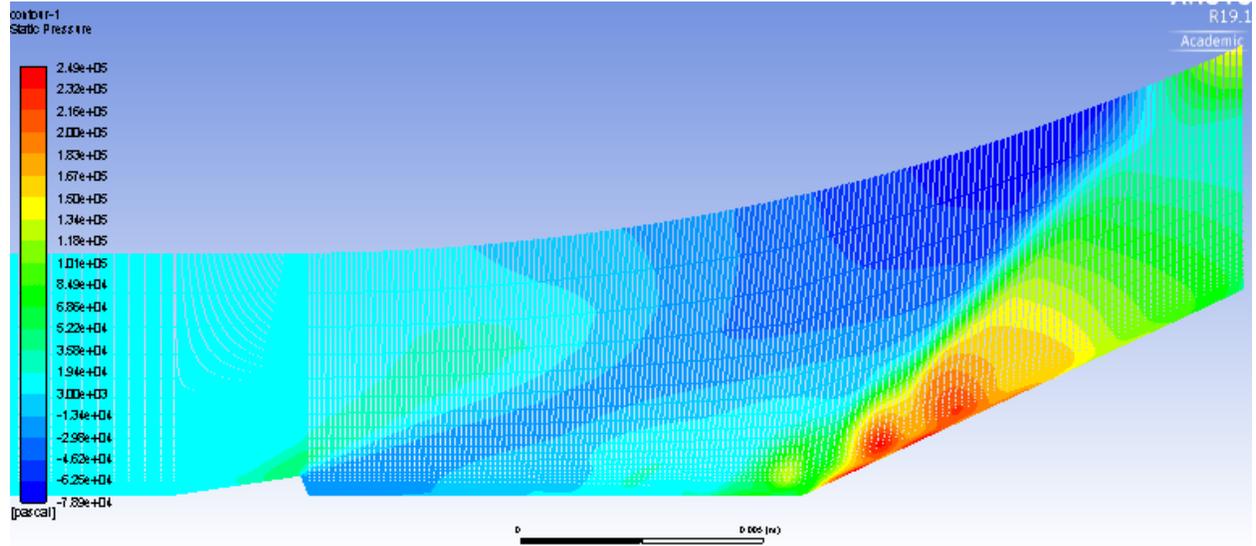
Figure B17 – The 2D, LES pressure contour plot results for the h/δ = 0.4 case.
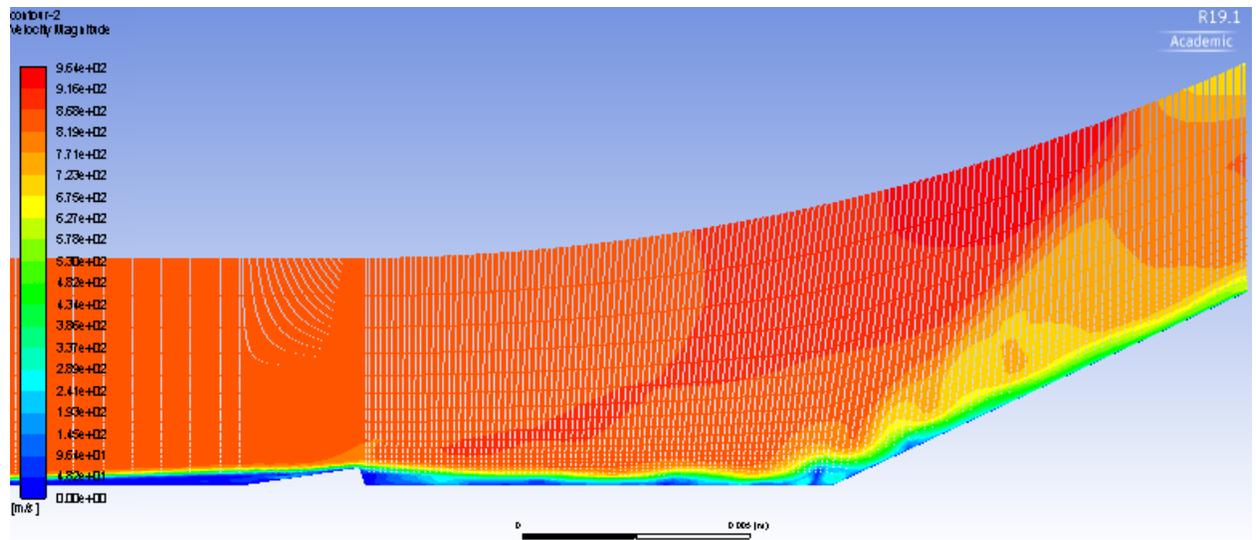
*Figure B18 – The 2D, LES velocity contour plot results for the h/δ = 0.4 case.*

h/δ = 0.5
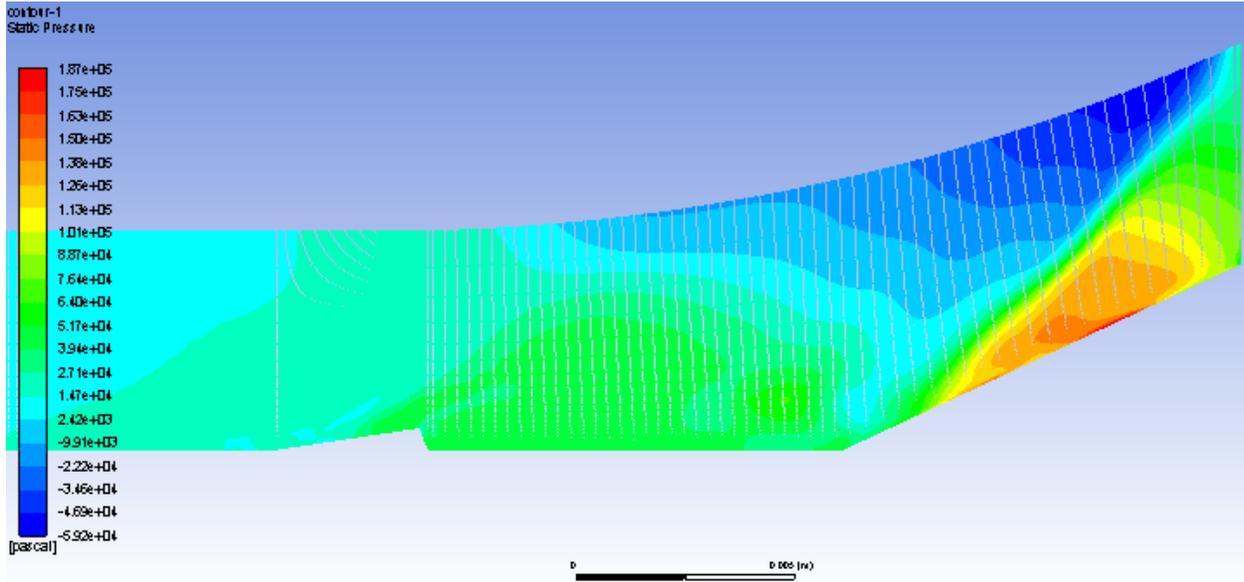
Figure B19 – The 2D, LES pressure contour plot results for the h/δ = 0.5 case.
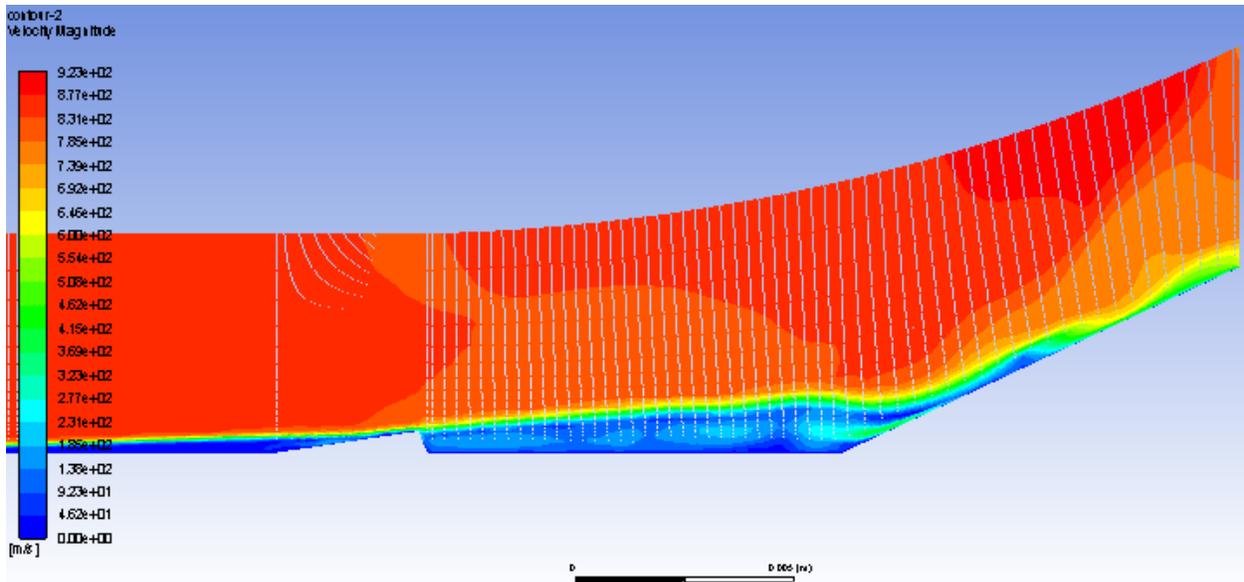
Figure B20 – The 2D, LES velocity contour plot results for the h/δ = 0.5 case.

h/δ = 0.6
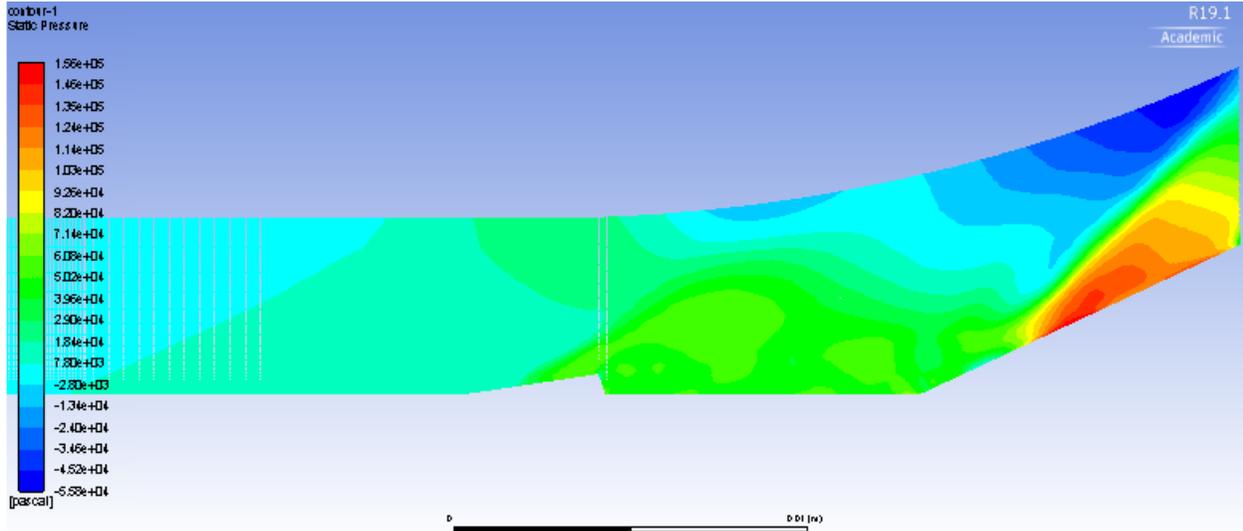
*Figure B21 – The 2D, LES pressure contour plot results for the h/δ = 0.6 case.*
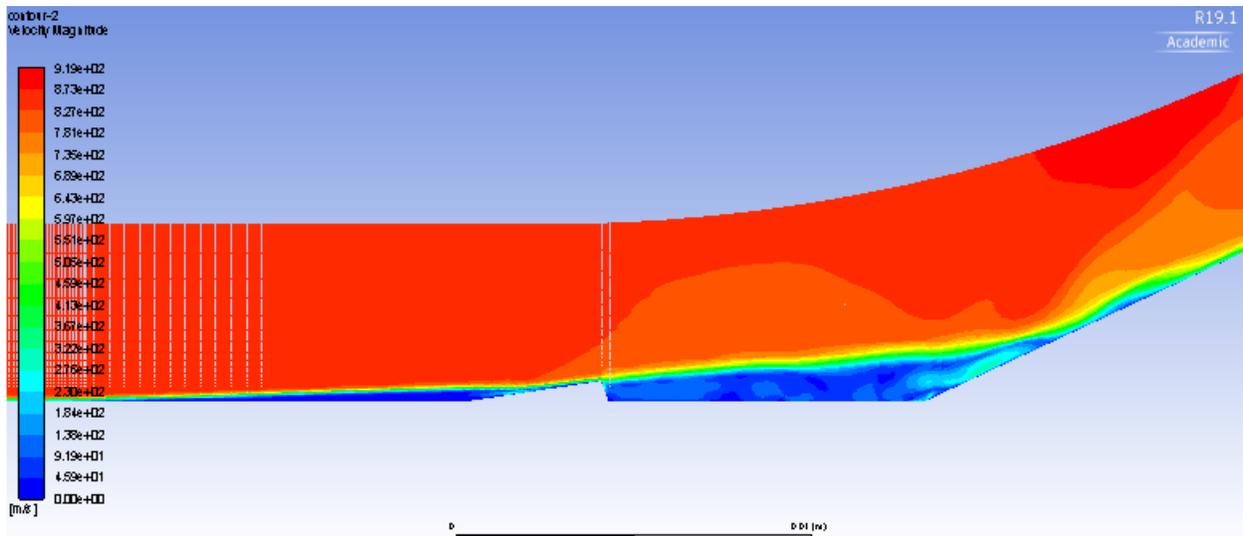
*Figure B22 – The 2D, LES velocity contour plot results for the h/δ = 0.6 case.*

h/δ = 0.7
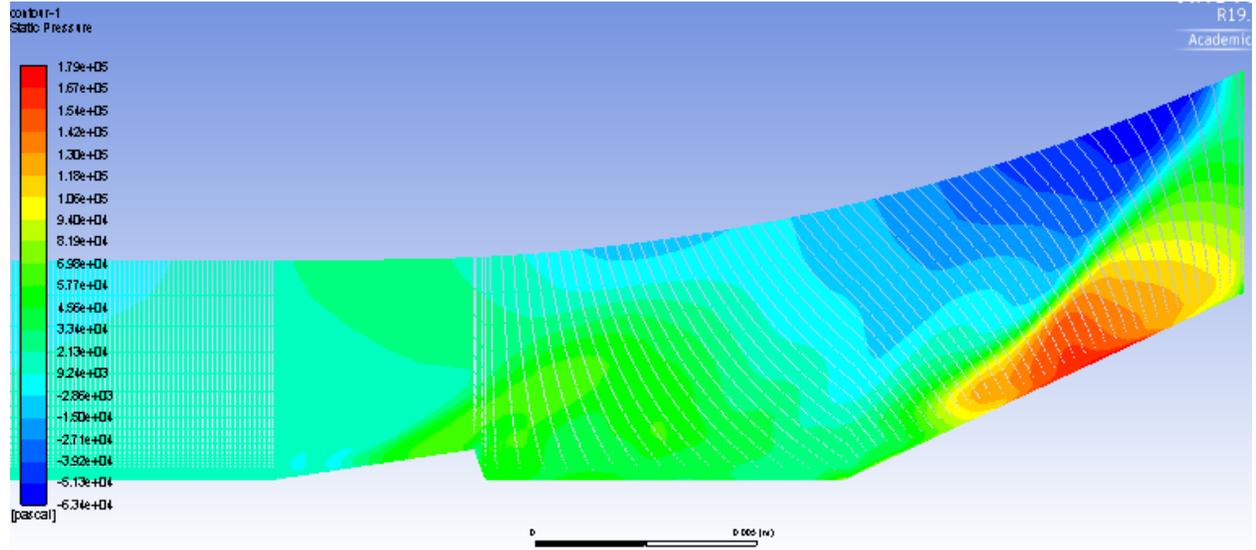
*Figure B23 – The 2D, LES pressure contour plot results for the h/δ = 0.7 case.*
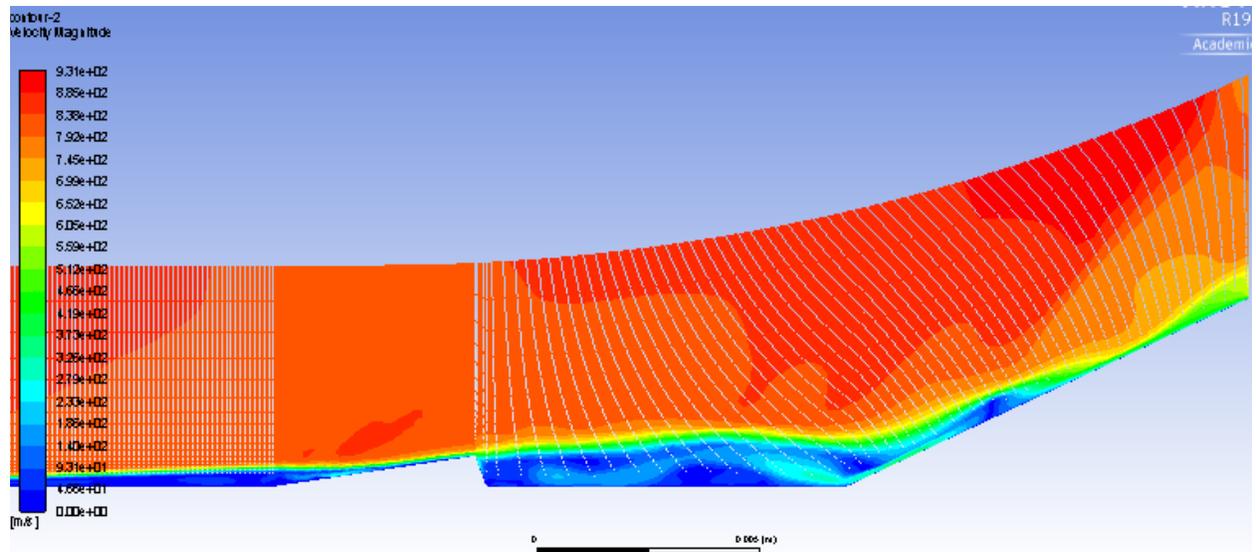
Figure B24 – The 2D, LES velocity contour plot results for the h/δ = 0.7 case.